

Phase-field modeling of complex interface dynamics in drop-laden turbulence

Alessio Roccon , Francesco Zonta , and Alfredo Soldati *Institute of Fluid Mechanics and Heat Transfer, TU-Wien, 1060 Vienna, Austria
and DPIA, University of Udine, 33100 Udine, Italy*

(Received 7 June 2023; accepted 8 August 2023; published 12 September 2023)

Turbulent flows laden with large, deformable drops are ubiquitous in nature and in a wide range of industrial processes. Prediction of the interactions between drops, which deform under the action of turbulence, exchange momentum via surface tension, and that can also exchange heat or mass, are complicated due to the wide range of scales involved: from the largest scales of the flow, down to the Kolmogorov scales of turbulence, and further down to the molecular scale of the interface. Due to this wide range of scales, the numerical description of these flows is challenging and requires robust and accurate numerical schemes that are able to capture both the turbulence characteristics and the dynamics of ever-moving and deforming interfaces including their topological changes (i.e., coalescence and breakage). In the past decades, various numerical methods have been proposed for simulating two-phase flows, from interface-tracking methods, where the interface is explicitly tracked with the use of marker points to interface-capturing methods, where the interface is identified as the isovalue of a color/marker function. Phase-field methods belong to the category of interface-capturing methods, and have emerged as promising approaches to simulate complex two-phase flows. In phase-field methods, the transport equation to describe the drop motion is obtained from first thermodynamics principles, and phenomena acting at the interface scale can be conveniently modeled. Although in realistic case scenarios, the physical thickness of the interface cannot be directly simulated, this family of methods offers desirable properties that have attracted the interest of researchers in recent years. In this work, we describe the fundamentals of the phase-field modeling associated with the direct numerical simulation of turbulence in the context of drop-laden flows. We discuss the potentials of the phase-field method with reference to breakage and coalescence phenomena, and to the corresponding drop size distribution; we examine how to model surface tension changes due to surfactant distribution, and we outline the framework to model heat and mass transfer fluxes. Finally, we present our perspectives for future developments of phase-field modeling of drop-laden turbulent flows in the context of the current available literature.

DOI: [10.1103/PhysRevFluids.8.090501](https://doi.org/10.1103/PhysRevFluids.8.090501)

I. INTRODUCTION

Turbulent multiphase flows are of great interest because of their importance in many natural and industrial applications, including rain formation [1], CO₂ absorption by breaking waves [2–4], hydrocarbon separation and drop/bubble-laden turbulent flows [5–9], or even host-to-host airborne disease transmission [10–12]. In all these phenomena, the dynamics of the interface, which can be locally influenced by the presence of surfactants and/or temperature gradients, crucially influences the entire process. Accurate experiments for multiphase flows are very complicated [13–15], and reliable simulations require sophisticated methods able to capture the topology of the different phases and their dynamics [5,7,16–18]. Nevertheless, simulations constitute an essential tool to investigate the physics of multiphase turbulence and are becoming increasingly popular in recent

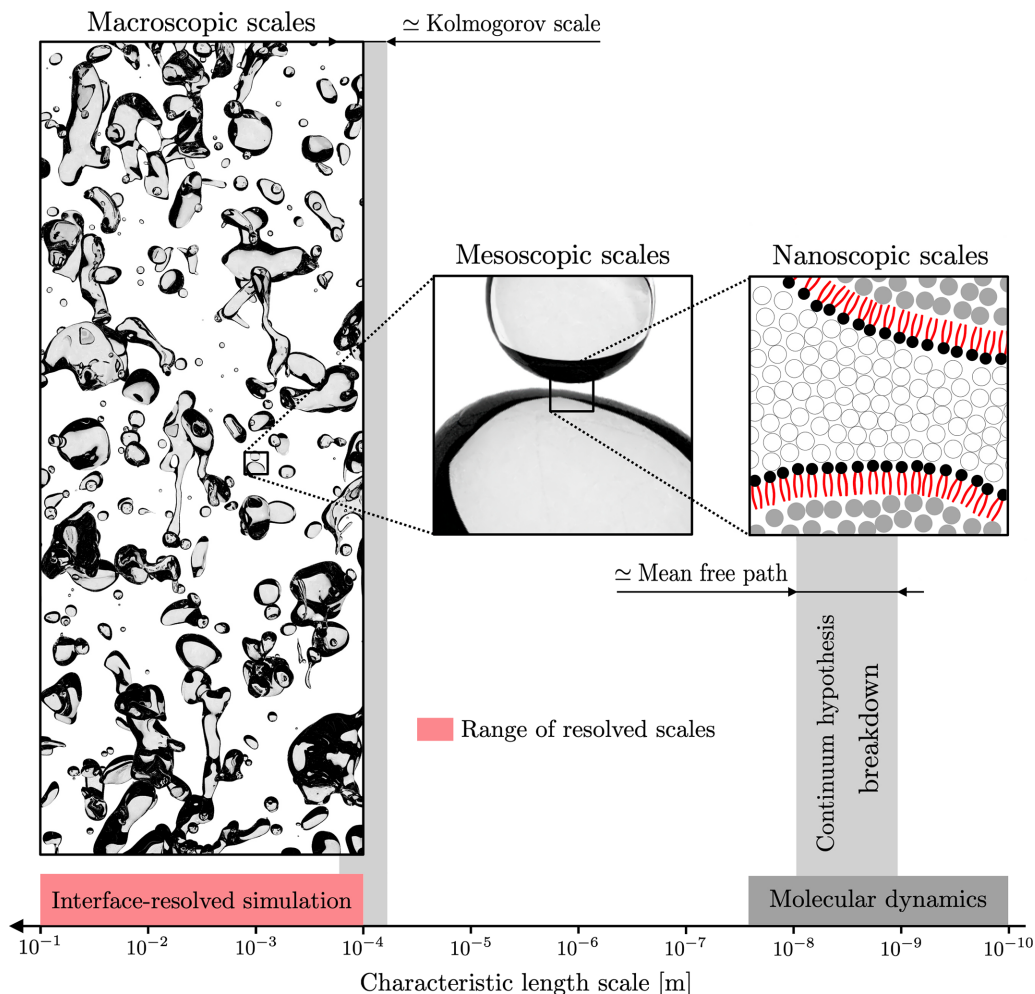


FIG. 1. Turbulent multiphase flows are characterized by a physics acting on a wide range of scales: from the largest integral scale of the problem (left side), down to the Kolmogorov scale (first close-up view) of turbulence and further down to the molecular scale of the interface (second close-up view). Depending on the range of resolved scales, we can distinguish among different approaches. We consider here interface-resolved simulation methods where interfacial structures (i.e., drops, bubbles, and ligaments) with a size similar to the flow field scales are resolved. In this type of simulations, phenomena occurring at the molecular scale of the interface cannot be directly resolved. Besides, it is also worth observing that capturing these phenomena require a different mathematical approach as at these small scales the continuum hypothesis breakdowns.

years: numerical simulations grant access to detailed space- and time-resolved information on the flow field, on the phases morphology (e.g., drops deformation) and on other quantities of interest (e.g., surfactant concentration, temperature fields).

Capturing the dynamics of a turbulent multiphase flow on a discretized temporal and spatial grid poses a further challenge, because of the huge scale separation that characterizes these kind of flows: scales range from the largest flow scale (of the order of the domain size, see Fig. 1, left side), down to the Kolmogorov scale of turbulence (first gray vertical stripe, from left to right, of Fig. 1) and further down to the molecular scale of the interface (see Fig. 1, right side). This has direct consequences on the representation of the physics of the system since there is a limit on

spatial and temporal resolution one can reasonably afford [19]. In particular, as done for single-phase turbulence [20–22], it would be highly desirable to perform simulations in which all scales are directly resolved, without any model. In fact, this approach cannot be applied to multiphase flows, since the scale separation between the largest flow scale and the smallest interfacial scale is about eight to nine orders of magnitude, while the most recent high-performance computing infrastructures (HPC), even exploiting the most recent advances in GPU computing [23], can handle a maximum scale separation of about three to four orders of magnitude. In addition, although most of the numerical approaches for the simulation of multiphase flows rely on the continuum hypothesis, as soon as length scales become smaller and smaller, the continuum hypothesis breaks down and molecular-scale dynamics must be considered [16,24–26].

The impossibility to resolve all the length scales using a unique set of governing equations has led to the development of different families of computational methods, which can be classified on the basis of the range of resolved scales and the characteristic size of the interfacial structures (e.g., drop, bubble, ligament) [5,7]. Here, we focus on the class of the interface-resolved methods, see Fig. 1. In this type of methods, the relevant interfacial structures (drops hereinafter without loss of generality) have a size comparable to that of the flow scales that are directly resolved, e.g., in most of the cases via direct numerical simulations (DNS). Interface-resolved methods can be divided into two big families: interface-tracking and interface-capturing methods. The fundamental difference lies in the definition of the interface: interface-tracking approaches explicitly follow the position of the interface with Lagrangian markers or interface-fitted meshes, while interface-capturing methods, the family to which the phase-field methods belong, define the interface position as a prescribed value of a color function or phase-concentration field. The definition of the interface has direct consequences on the simulation of topological changes of the interface (as, for instance, breaking and merging): interface-tracking methods require explicit models to manage the connectivity of Lagrangian markers or meshes, while interface-capturing methods handle implicitly topological modifications of the interface.

The phase-field methods are a class of mathematical models built upon the pioneering works of van der Waals [27], Ginzburg and Landau [28,29], and Cahn and Hilliard [30–33]. These methods are based on the definition of an Eulerian field, the phase-field ϕ , which is a function of position and time, to describe the interface position between different regions (or states) of the domain. These regions can be representative of different gas/liquid phases, types of material microstructure, solid/liquid material states, fractured/nonfractured regions, depending also on the considered application. The interface between two regions is described by a smooth, but highly localized, change of the phase variable between two fixed values. For computational reasons, the thickness of this thin interfacial layer is typically larger than the physical width of an actual interface. Indeed, the thickness of this thin interfacial layer is used as a parameter for numerical convenience and it is usually set as small as possible but compatibly with the computational resources available. As mentioned above, the field of applications of the phase-field method is vast and cannot be detailed in a single article. Examples of applications of the phase-field method are: multiphase flows (object of this work) [7,18,34–36], solid-liquid transformations (e.g., phase-change materials, ice-melting) [37–39], modeling of active matter and systems [40–42], microstructure and solidification [43–47], fracture of materials [48–50], study of metallic foams [51,52] as well as many others [53,54]. The reader is referred to previous reviews [36,43,45,55,56] for specific information on the phase-field methods and their applications.

Phase-field methods have emerged as promising approaches for simulating two-phase flows and, especially in the past decade, they gained popularity thanks to the availability of improved formulations that resolve some drawbacks of the original formulations. The first work in which the phase-field method is proposed as a possible approach for simulating two-phase flow traces back to the pioneering work of Jacqmin [57], who used the phase-field method to study the Rayleigh-Taylor instability. This work laid the foundation for the use of the phase-field method in multiphase flow simulations. Building on top of this seminal work, different phase-field method formulations and numerical techniques, either based on the Cahn-Hilliard equation or Allen-Cahn

equation have been developed and used to analyze different flow instances: drop-laden turbulent flows [58–63], bubble-laden turbulent flows [58,64], emulsions [65,66], two or multilayer turbulent flows [67–69], microdevices [70], spinodal decomposition [71–74], drop-substrates interactions and wetting phenomena [75–77], Rayleigh-Taylor and Rayleigh-Bénard configurations [57,78,79]. Going beyond immiscible two-phase flows, the phase-field method has been also used to describe more complex types of flows. For the description of surfactant-laden interfaces, extensions of the phase-field method, which involve the use of additional scalar functions, have been proposed for soluble surfactants [80–83]. The transport of passive/active scalars, like temperature or species concentration, in multiphase turbulence can be easily accounted for in the context of phase-field methods [79,84,85]. Recently, ad hoc formulations have been proposed for the study of phase change problems, from solid-liquid [38,39] to evaporation/boiling phenomena [86–88]. Finally, phase-field methods have been also used to describe the dynamics of solid finite size particles [89] or particle-interface interactions [90,91].

The paper is organized as follows: in Sec. II, we present the fundamentals of the phase-field methods briefly reviewing the governing equations and different formulations available. In Sec. III, we describe the coupling with the Navier-Stokes equations detailing two important aspects of drop- and bubble-laden turbulent flows: the modeling of surface tension forces and the handling of density and viscosity contrasts. In Sec. IV, we describe the capabilities and limitations of the phase-field method in describing multiphase turbulence. Then, in Sec. V, we describe the challenges associated with the description of more complex flows which involve the transfer of heat, mass and chemical compounds (e.g., surfactants). Finally, in Sec. VI, we discuss the future perspectives and we draw the conclusions.

II. PHASE-FIELD MODELING OF INTERFACIAL PHENOMENA

Phase-field methods belong to the class of interface-capturing methods. These methods rely on the use of a color function, in this case the phase-field ϕ , to define the instantaneous interface position. The phase field is transported by a proper governing equation [30–32,92,93] and can be exploited to compute different quantities of interest of two-phase flows, as for instance the local interface curvature [92,94], thermophysical properties [36,63,64,95,96], signed distance from the interface [91], other geometric properties of the interface [97], etc. With respect to other commonly employed interface-capturing methods like volume-of-fluid methods [98], in phase-field methods, the color function does not abruptly change moving from one phase to another, but instead undergoes a continuous transition in a thin interfacial layer [99,100]. This property of phase-field methods offers some unique advantages that range from an accurate computation of the interface curvature to ease of coupling with more complex physics (e.g., surfactant-laden interfaces [83], solid particles [101], contact-angle dynamics [102]).

Phase-field methods are traditionally based on Cahn-Hilliard [30–32] or Allen-Cahn [33] equations, Fig. 2. These two governing equations are obtained as gradient flows of a Ginzburg-Landau free-energy functional, which can be defined as follows:

$$\mathcal{F}[\phi, \nabla\phi] = \int_{\Omega} \left(\underbrace{\frac{(\phi^2 - 1)^2}{4}}_{f_0} + \underbrace{\frac{\epsilon^2}{2} |\nabla\phi|^2}_{f_{\text{mix}}} \right) d\Omega, \quad (1)$$

where Ω is the domain considered, ϵ is a capillary width that controls the extension of the transition layer, and ϕ is the phase field (equal to $\phi = \pm 1$ in the two pure phases) [103]. The functional is composed by the sum of two contributions, the double-well potential, f_0 , accounting for the separation of the two phases (phobic behavior) and the mixing term, f_{mix} , accounting for the energy stored at the interface (i.e., surface tension). From the free-energy functional, the chemical potential

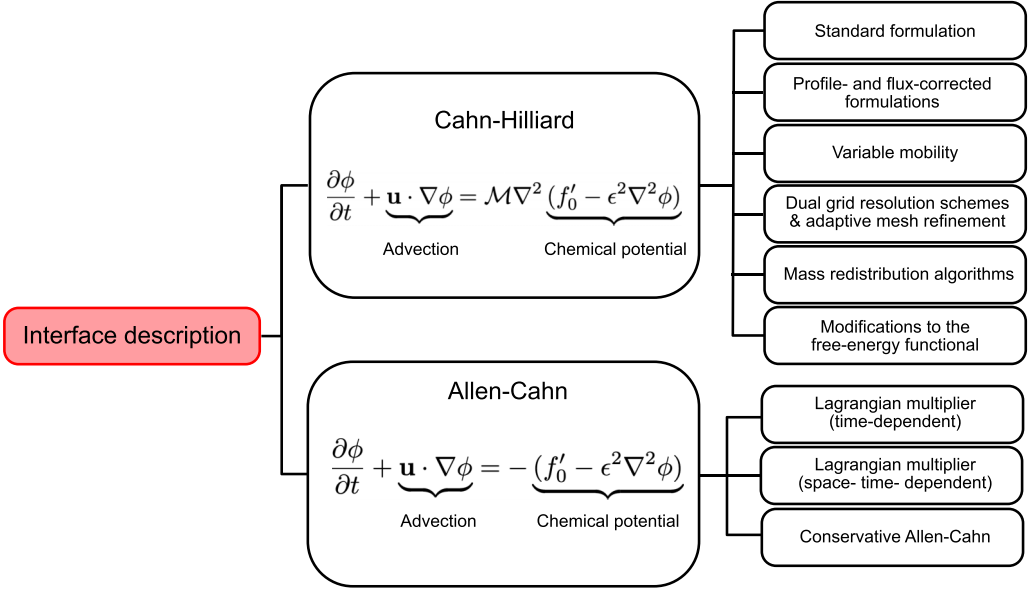


FIG. 2. Phase-field method formulations available for the description of multiphase flows at a glance. We can distinguish between formulations that rely on the Cahn-Hilliard equation—a conservative fourth-order equation—and Allen-Cahn equation—a second-order equation that in its original form is not conservative. For Cahn-Hilliard-based phase-field methods, in addition to the standard formulation, mass-conservation improved alternative approaches are available: (i) profile- and flux-corrected formulations; (ii) approaches that employ variable mobility coefficients; (iii) use of dual grid resolution methods and adaptive mesh refinement; (iv) mass-redistribution algorithms; (v) use of modified free-energy functionals. For Allen-Cahn-based phase-field methods, different methods are available to conserve the phase-field variable: (i) use of time-dependent Lagrangian multipliers; (ii) use of space- and time-dependent Lagrangian multipliers; (iii) conservative version of the Allen-Cahn equation.

can be obtained as the functional derivative:

$$\mu_\phi = \frac{\delta \mathcal{F}[\phi, \nabla \phi]}{\delta \phi} = f'_0 - \epsilon^2 \nabla^2 \phi, \quad (2)$$

where f'_0 denotes the derivative of f_0 with respect to ϕ . From the chemical potential expression, we can obtain the equilibrium profile for a planar interface by solving the equation $\nabla \mu_\phi = \mathbf{0}$. The solution for a planar interface is

$$\phi_{eq} = \tanh\left(\frac{s}{\sqrt{2}\epsilon}\right), \quad (3)$$

where s is the coordinate normal to the interface. From Eq. (2), the Cahn-Hilliard and Allen-Cahn equations can be derived as the $H^{-1}(\Omega)$ and $L^2(\Omega)$ gradient flows of the free-energy functional, respectively. In the absence of flow-field advection, the Cahn-Hilliard equation reads as follows:

$$\frac{\partial \phi}{\partial t} = \nabla^2 (f'_0 - \epsilon^2 \nabla^2 \phi), \quad (4)$$

while the Allen-Cahn equation is

$$\frac{\partial \phi}{\partial t} = \epsilon^2 \nabla^2 \phi - f'_0. \quad (5)$$

Here, two important characteristics that make these two equations different can be appreciated. First, we observe that the Cahn-Hilliard equation is a fourth-order partial differential equation, while the Allen-Cahn equation is a second-order equation. Second, by imposing no-flux conditions at the domain boundaries, Cahn-Hilliard equation leads to the conservation of the phase field, while the Allen-Cahn equation does not. These two equations represent the building blocks of almost all phase-field formulations. We can distinguish between two macroclasses of phase-field methods. In the first class of phase-field methods, also known as energy-based phase-field methods, the phase field is governed by a Cahn-Hilliard equation, a fourth-order equation that, as already mentioned, satisfies global mass conservation. In the second class of phase-field methods, also known as second-order phase-field methods, the phase-field is governed by an Allen-Cahn equation, a second-order equation that in its original form does not satisfy global mass conservation, but that can be modified so to fulfill this constraint. Before proceeding, it is important to remark that conservation of the global mass does not guarantee the conservation of the individual mass of each phase [104,105]. For a detailed discussion of this point, the interested reader is referred to Appendix A. In the next two sections, Cahn-Hilliard- and Allen-Cahn-based approaches will be discussed.

A. Cahn-Hilliard-based phase-field methods

This class of phase-field methods is based on the Cahn-Hilliard equation. Starting from the original formulation of the Cahn-Hilliard equation and including the flow-field advection, we obtain the following equation:

$$\frac{\partial \phi}{\partial t} + \mathbf{u} \cdot \nabla \phi = \mathcal{M} \nabla^2 (f'_0 - \epsilon^2 \nabla^2 \phi), \quad (6)$$

where $f'_0 = \phi^3 - \phi$ denotes the first derivative of f_0 with respect to ϕ and \mathcal{M} is the mobility parameter. Expanding the right-hand side, we can observe that the equation is a fourth-order equation and particular care should be taken in choosing the numerical method. Despite this, in recent years, schemes for the solution of the Cahn-Hilliard equation have been developed employing finite-difference [58,106], finite volume/element [107], Lattice-Boltzmann [108,109], and pseudospectral methods [99,110]. Thanks to its conservative nature and robustness, the Cahn-Hilliard equation has been widely used in simulating two-phase flow. In addition, given the smoothed nature of the phase-field variable, the interface curvature can be accurately computed and thermophysical properties can be assumed to be proportional to the phase field, avoiding the use of additional smoothing kernels to smear out density and viscosity variations. Finally, since the Cahn-Hilliard equation is obtained as the gradient flow of a free-energy functional, the hyperbolic tangent profile across the transition layer comes directly from the energy minimization principle without the need for reinitialization schemes.

The use of realistic parameters for the Cahn-Hilliard equation is however not feasible from a computational point of view: since in numerical simulations the transition layer must be numerically discretized, the adoption of realistic values for the capillary width ϵ —order of nanometers—is not possible. This possibly leads to some drawbacks, usually referred to as shrinkage and coarsening effects, when the method is applied to simulations of immiscible two-phase flows. To overcome these issues, different strategies, which are briefly discussed in the following, have been developed.

A first possible strategy is the use of penalty fluxes q_c , which further enforce the equilibrium profile [105,111,112]:

$$\frac{\partial \phi}{\partial t} + \mathbf{u} \cdot \nabla \phi = \mathcal{M} \nabla^2 (f'_0 - \epsilon^2 \nabla^2 \phi) + q_c, \quad (7)$$

Examples of this strategy are the profile-corrected [111] and flux-corrected formulations [112]. A second strategy foresees the use of variable or degenerate mobility coefficients [113–116]. The

Cahn-Hilliard equation is thus modified as follows:

$$\frac{\partial \phi}{\partial t} + \mathbf{u} \cdot \nabla \phi = \nabla \cdot [\mathcal{M}(\phi) \nabla (f'_0 - \epsilon^2 \nabla^2 \phi)], \quad (8)$$

where $\mathcal{M}(\phi) = \mathcal{M}_0(1 - \gamma^2 \phi^2)$ is the variable mobility and $0 \leq \gamma \leq 1$ is a positive coefficient. For $\gamma = 1$ (degenerate mobility), bulk diffusion vanishes in the bulk and diffusion occurs only in the interfacial layer. A third possible approach involves the use of dual grid resolution methods [58,117], which employ a finer grid resolution to resolve the Cahn-Hilliard equation compared to that used for the velocity and pressure fields, or the use of adaptive mesh refinement algorithms, which locally refine the mesh in the interfacial region [118–122]. Another viable solution foresees the use of mass redistribution algorithms [123], which have been also used in the context of Allen-Cahn-based models [124]:

$$\frac{\partial \phi}{\partial t} + \mathbf{u} \cdot \nabla \phi = \mathcal{M} \nabla^2 (f'_0 - \epsilon^2 \nabla^2 \phi) + q_m, \quad (9)$$

where q_m is the source term introduced to compensate for shrinkage and coarsening effects [123]. Finally, modifications to the free-energy functional [125,126] aimed at removing the curvature-driven interface motion obtained when drops and bubbles with nonzero curvature are described can be also adopted:

$$\mathcal{F}[\phi, \nabla \phi] = \int_{\Omega} \left(\frac{(\phi^2 - 1)^2}{4} + \frac{\epsilon^2}{2} |\nabla \phi|^2 + f_c \right) d\Omega, \quad (10)$$

where f_c is the additional contribution included in the energy functional. Likewise, the resulting chemical potential (obtained as the functional derivative of the energy functional reported above) is also modified. These modifications resemble the procedure used to derive the conservative Allen-Cahn equation by subtracting the curvature-driven motion [92,124,127] (see Appendix B for details).

B. Allen-Cahn-based phase-field methods

This class of phase-field methods is based on the Allen-Cahn equation [33]. Starting from the original formulation of the Allen-Cahn equation, Eq. (5), and including the flow-field advection, we obtain

$$\frac{\partial \phi}{\partial t} + \mathbf{u} \cdot \nabla \phi = -(f'_0 - \epsilon^2 \nabla^2 \phi) = \epsilon^2 \nabla^2 \phi - f'_0, \quad (11)$$

where f'_0 denotes the first derivative of f_0 with respect to ϕ . The Allen-Cahn equation is a second-order equation that has been widely used in material science applications involving melting, solidification, and state transformation changes [43,56]. Due to its nonconservative nature, the Allen-Cahn equation cannot be directly used in this form for simulations of two-phase flows with no phase change. However, compared to the Cahn-Hilliard equation, Allen-Cahn is simpler from a mathematical point of view as it is a second-order equation for which a large number of fast and efficient numerical methods are available, like finite difference [96,128,129] and Lattice-Boltzmann schemes [130–135]. This has motivated researchers to modify the nature of this equation to make it appealing for simulations of two-phase flows. A common strategy involves the use of local and nonlocal corrections using Lagrangian multipliers [136–143] to enforce the conservation of the phase field. For time-dependent multipliers, the Allen-Cahn equation is modified as follows:

$$\frac{\partial \phi}{\partial t} + \mathbf{u} \cdot \nabla \phi = \epsilon^2 \nabla^2 \phi - f'_0 + \beta(t); \quad \beta(t) = \frac{\int_{\Omega} f'_0 d\Omega}{\int_{\Omega} d\Omega}, \quad (12)$$

where $\beta(t)$ is the time-dependent Lagrangian multiplier (i.e., the nonlocal correction). For space- and time-dependent Lagrangian multipliers the Allen-Cahn equation reads as follows:

$$\frac{\partial \phi}{\partial t} + \mathbf{u} \cdot \nabla \phi = \epsilon^2 \nabla^2 \phi - f'_0 + \sqrt{2f_0} \beta(t); \quad \beta(t) = \frac{\int_{\Omega} f'_0 d\Omega}{\int_{\Omega} \sqrt{2f_0} d\Omega}, \quad (13)$$

where the term $\sqrt{2f_0} \beta(t)$ is a space- and time-dependent Lagrangian multiplier. In general, the use of space- and time-dependent Lagrangian multipliers provide better performance and allow for the description of small interfacial features [138,144,145], which otherwise might dissolve in the bulk [144].

Another viable approach involves the use of local modifications of the PDE [92,127,146]. In particular, considering that the right-hand side of the Allen-Cahn equation describes a curvature-driven motion (see Appendix B for details), Chiu and Lin [124] derived, following the idea of subtracting the curvature-driven interfacial motion developed by Sun and Beckermann [92], the conservative version of the Allen-Cahn equation [147]:

$$\frac{\partial \phi}{\partial t} + \nabla \cdot (\mathbf{u}\phi) = \gamma \nabla \cdot \left[\left(\sqrt{2\epsilon} \nabla \phi - (1 - \phi^2) \frac{\nabla \phi}{|\nabla \phi|} \right) \right], \quad (14)$$

where $\mathbf{n} = \nabla \phi / |\nabla \phi|$ is the interface normal vector. On the right-hand side of Eq. (14), we can recognize a diffusive term and a sharpening term, which is used to maintain the hyperbolic tangent profile of the transition layer and to conserve the phase field. Interestingly, the right-hand side of Eq. (14) matches, up to coefficients, the expression of the penalty-flux term in the profile- and flux-corrected formulations of the phase-field methods [105,111,112] (see also Sec. II B). Note also that Eq. (14) shares some similarities with the conservative level-set method [148–153], for example, the use of a hyperbolic tangent kernel and of diffusive and sharpening fluxes to conserve the phase indicator. The main difference between the two methods lies in the number of steps required to compute the phase indicator: two for the conservative level-set method (advection and reinitialization) and one for the conservative phase-field method [93,124]. Finally, it is worth observing that by removing the curvature-driven motion present in the original Allen-Cahn equation, the resulting equation is not anymore the gradient flow of a free-energy functional and equation (14) can be also derived from pure geometrical considerations [92,124,150]. In this case, the hyperbolic tangent profile of the interface is an advected kernel rather than a solution obtained from thermodynamic considerations. For this reason, these formulations are also referred to as advected phase-field methods [70,150]. This type of phase-field methods have recently attracted the attention of many researchers thanks to their ease of implementation and favorable properties, e.g., the boundedness of the phase-field solution [93,154]. Possible improvements have been recently proposed by Jain *et al.* [155], who modified the sharpening term replacing the phase field with the signed distance from the interface, so to obtain a more regular function that does not contain any jumps/discontinuities.

III. FLOW-FIELD DESCRIPTION

The description of the flow field requires methodologies that can handle the jump conditions at the interface imposed by the surface tension forces and the difference in density and viscosity between the two phases [17]. For the sake of simplicity, here we consider only the one-fluid approach (or whole-domain approach). This approach is based on the solution of a single set of Navier-Stokes equations in the entire domain (usually performed on a structured grid) and accounts for the interfacial jump conditions (i.e., continuity of velocity and viscous stress and surface tension pressure jump) via the introduction of source terms. The one-fluid approach is the oldest and most widely used one because fast and efficient single-phase flow solvers can be adapted for the purpose without the need of extensive modifications. Possible alternatives to this approach are: (i) body-fitted grid methods [156–159], which rely on the solution of multiple sets of Navier-Stokes equations, one for each phase, coupled at the interface; (ii) ghost-fluid methods [160–165], which rely on the

solution of the Navier-Stokes equations in separated domains using structured grids and employ ghost nodes to couple the different domains. In the context of the one-fluid approach, a single set of Navier-Stokes equations is solved in the entire domain. If we consider the mixture of two immiscible, incompressible, and Newtonian phases, then the resulting Navier-Stokes equations in conservative form read as follows:

$$\nabla \cdot \mathbf{u} = 0, \quad (15)$$

$$\frac{\partial(\rho\mathbf{u})}{\partial t} + \nabla \cdot (\rho\mathbf{u} \otimes \mathbf{u}) = -\nabla p + \nabla \cdot [\eta(\nabla\mathbf{u} + \nabla\mathbf{u}^T)] - \sigma\kappa\mathbf{n}\delta, \quad (16)$$

where $\mathbf{u} = (u, v, w)$ is the velocity vector, p is the pressure field, ρ and η are the density and viscosity fields, respectively and in general are functions of the phase-field variable. The last term at the right-hand side of Eq. (16) represents the contribution of the surface tension forces, with σ the surface tension, κ the mean curvature, \mathbf{n} the interface normal vector, and δ the surface Dirac δ that identifies the interface location [166]. The use of the conservative form of the Navier-Stokes equations (as reported above) is in general recommended, especially when local methods are employed. This is however just one of the requirements to obtain an accurate and robust simulation method [96]. Compared to the single-phase version of the Navier-Stokes and continuity equations obtained assuming constant and uniform density and viscosity, Eqs. (15) and (16) are characterized by two main features: (i) a source term that accounts for the surface tension pressure jump that arises at the interface; (ii) the presence of density and viscosity contrasts. The modeling of interfacial forces and density/viscosity contrasts represents the crucial aspect of the development and use of accurate methodologies for multiphase flow simulations. In the two following sections, these two aspects will be addressed in detail.

A. Modeling surface tension forces

Surface tension forces, which arise at the interface between two fluids, and are due to the cohesive interactions between molecules and the associated energy, are proportional to the surface tension value and to the local curvature. If the surface tension is constant, then surface tension forces act along the direction normal to the interface. In principle, the best approach to account for these forces, which are localized at the interface, is to use conformal meshes and integral formulations. This approach is computationally very expensive and therefore of scarce applicability. Most large-scale simulations are usually performed using Eulerian methods, and thus the common choice is to use volumetric formulations, which are based on a numerical approximation of the Dirac function to account for surface tension forces [167,168]. Therefore, interfacial forces are approximated as follows:

$$\mathbf{f}_\sigma = -\sigma\kappa\mathbf{n}\delta_s = \sigma\nabla \cdot [(\mathbf{I} - \mathbf{n} \otimes \mathbf{n})\delta_s], \quad (17)$$

where δ_s is a smoothed Dirac δ . The first expression is the building block of the continuum surface force (CSF) model [169], while the second is the building block of the continuum surface stress (CSS) model [16,170,171]. In the CSF formulation, originally applied to volume-of-fluid [169,171] and level-set [172] methods, the δ function is approximated using a Heaviside function. A similar approach can be employed also for phase-field methods [173]. The normal vector and the curvature required to evaluate the interfacial forces [equation (17)] can be directly computed from the phase field [92]:

$$\mathbf{n} = \frac{\nabla\phi}{|\nabla\phi|}; \quad \kappa = \nabla \cdot \mathbf{n}. \quad (18)$$

Phase-field methods can provide accurate computation of the curvature thanks to the smoothness of the phase-field variable ϕ , while volume-of-fluid methods normally require convolution operations [174], height function approaches [175–177], or higher-order interface reconstruction methods [178,179]. Accurate computation of curvature is crucial for accurate computation of surface tension

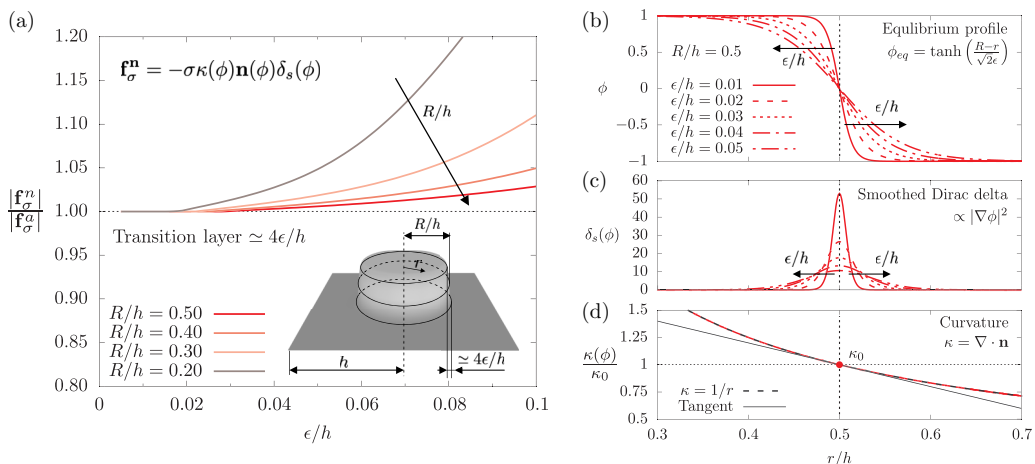


FIG. 3. Panel (a) shows the ratio between the numerical value of the surface tension forces, $|\mathbf{f}_\sigma^n|$, and the analytical one, $|\mathbf{f}_\sigma^a|$ (in magnitude). Results are shown for different dimensionless capillary widths ϵ/h and droplet radii: $R/h = 0.5$ (red), $R/h = 0.4$ (light red), $R/h = 0.3$ (orange), and $R/h = 0.2$ (gray); length scales are reported normalized by the half-length of the computational domain, h . Surface tension forces are computed using a CSF approach on a Cartesian grid using finite differences. The behavior of the equilibrium profile, smoothed Dirac δ , and curvature are reported in panels (b–d) for a droplet with radius $R/h = 0.5$ and different capillary widths ϵ/h . In general, a good approximation of the surface tension forces is obtained. The overestimation of surface tension forces obtained for large capillary widths can be traced back to the following drawback: As the phase field is a smooth field, the curvature is defined everywhere in the domain and corresponds to the local curvature of the isocontour (d). However, the curvature $\kappa(\phi)$ is in general different from the one corresponding to the isolevel $\phi = 0$, i.e., $\kappa_0 = \kappa(\phi = 0)$. This leads to an overestimation when large capillary widths ϵ/h are considered and the smoothed Dirac δ samples a wide range of curvature values.

forces, and in the next example we show the robustness of phase field to compute surface tension forces for different grid resolutions. In particular, in Fig. 3 we show the effect of changing the thickness of the transition layer on the computation of the interface forces. In this specific example, we consider the simple case of a two-dimensional drop in quiescent fluid and we vary the grid resolution: in this way, we change the thickness of the transition layer, which is proportional to the capillary width, i.e., it is $4\epsilon/h$. In Fig. 3(a) we show the numerical values of the surface tension forces, $|\mathbf{f}_\sigma^n|$, computed using a CSF approach. These values are obtained for different dimensionless droplet radii R/h and capillary widths ϵ/h (with h the half-length of the computational domain) and are normalized by the value, $|\mathbf{f}_\sigma^a| = \sigma\kappa\mathbf{n}$, which is analytically computed for a thickness of the transition layer tending to zero. We can observe that surface tension forces are accurately evaluated for a wide range of capillary width ϵ and droplet radii, even when the transition layer has a characteristic size comparable with the droplet radius, i.e., when $4\epsilon/h \simeq R/h$. The discrepancy between analytical and numerical values obtained for small droplet radii and large capillary widths is due to the fact that the curvature is defined everywhere in the domain [Eq. (18)], and represents the curvature of the local isocontour of ϕ [168,180], see Fig. 3(d). This curvature, which is not uniform in space and is in general slightly different from that corresponding to the drop interface—defined as $\kappa_0 = \kappa(\phi = 0)$ (i.e., of the isolevel $\phi = 0$)—leads to an overestimation of surface tension forces when large capillary widths ϵ/h are considered, since the smoothed Dirac δ centered at the reference interface location [Fig. 3(c)] samples a wide range of curvature values [see the higher-than-linear behavior of curvature in Fig. 3(d)]. The accuracy of the CSF approach, which is at best first-order, limits its applicability in surface tension-dominated flows [19,168]. Better results can be obtained

using the energy-based (EB) formulation [181], which relies on the chemical potential definition to compute surface tension forces. This formulation, analytically equivalent to the CSS approach, does not involve the direct computation of the interface curvature. Rather, the calculation of surface tension forces is based on the smooth equilibrium profile and on the chemical potential definition. The resulting order of accuracy is in general higher than that obtained using CSF-based approaches [181] and extensions of this approach have been also applied to level-set methodologies [182,183]. To compute accurately the interfacial forces, the interfacial transition profile should be as close as possible to the equilibrium kernel. In general, the energy-based approach is best suited for interfaces characterized by uniform surface tension. Although this approach can be extended to surfactant-laden interfaces [82,184], the surfactant effect on surface tension cannot be modified, and tangential contribution cannot be easily separated from normal one [83,185] as when CSF/CSS approaches are employed.

Finally, regardless of the approach used to compute surface tension forces, balanced numerical schemes should be preferred [186]. This is usually achieved by a consistent discretization of pressure gradients terms and surface tension forces, so to match the equilibrium solution given by the Laplace equation for a spherical drop: $\Delta p = \kappa\sigma = 2\sigma/R$. The use of schemes that do not satisfy this requirement can lead to the generation of spurious currents, i.e., artificial currents generated by unbalanced forces at the interface [168]. Quite often, the presence of these currents is by no means negligible, and can even overwhelm the underlying physics of the system, making the interpretation of the simulation results challenging. The consequences of spurious currents can be far-reaching, leading not only to the incorrect predictions of the flow behavior, but also to the misrepresentation of heat/mass transfer fluxes, in particular when the role played by surface tension forces is important [170]). Not surprisingly, mitigation of spurious currents can be obtained via improved calculations of interface curvature (for example, better pressure and surface tension discretization, smoother phase indicators, use of height functions in VOF [178,187,188]).

To give an example of spurious currents, we consider the case of a two-dimensional static drop having diameter $R/h = 0.4$ [with h the half-size of the domain, see the sketch reported in the inset of Fig. 3(a)] immersed in a quiescent fluid. The governing equations have been discretized using a pseudospectral approach (see Soligo *et al.* [83] for details). The domain has size $2h \times 2h$, and the results are obtained using a phase-field method and different approaches for the computation of the surface tension forces: (i) continuum-surface force approach (CSF); (ii) continuum-surface stress (CSS); (iii) energy-based or chemical potential-based method (EB). Simulations are run considering a fixed value of the surface tension and of the capillary width $\epsilon/h = 0.04$ (i.e., of the thickness of the transition layer), but different grid resolutions: from 32×32 up to 256×256 , thus corresponding to different values of the grid spacing $\Delta = 2h/N$. Simulations are run until a stationary, equilibrium state is achieved. In Fig. 4(a), we visualize contour maps of the L_∞ norm of the velocity field, $\|\mathbf{u}\|_\infty$. As apparent, the velocity field is not perfectly zero everywhere as it should be (at least down to machine accuracy), but spurious currents, whose magnitude depends on the grid spacing and on the approach used to compute surface tension forces, are present in a thin layer around the interface (which is explicitly rendered by the circular black line). Note that the technique employed for the space discretization can have an impact on the magnitude of spurious currents: in the present case, the use of a pseudospectral technique induces low spurious currents, which can become a bit higher when other discretization techniques (for example finite differences) are used [189]. A more quantitative evaluation of the magnitude of spurious currents is provided in Fig. 4(b), where the numerical values of $\|\mathbf{u}\|_\infty$ are reported as a function of the grid resolution $\Delta = 2h/N$, for the different cases discussed here. In general, it can be observed that better results in terms of spurious currents can be obtained using the CSS and the EB approaches. Both approaches avoid the direct computation of the curvature from the phase-field variable and thus provide overall better performance. We can also observe that the order of convergence is higher for CSS and EB approaches. Specifically, while the CSF approach is approximately first-order accurate, the CSS and EB approaches are second- and third-order order accurate, respectively [see the triangles showing the scaling slope on the left-hand side of Fig. 4(b)].

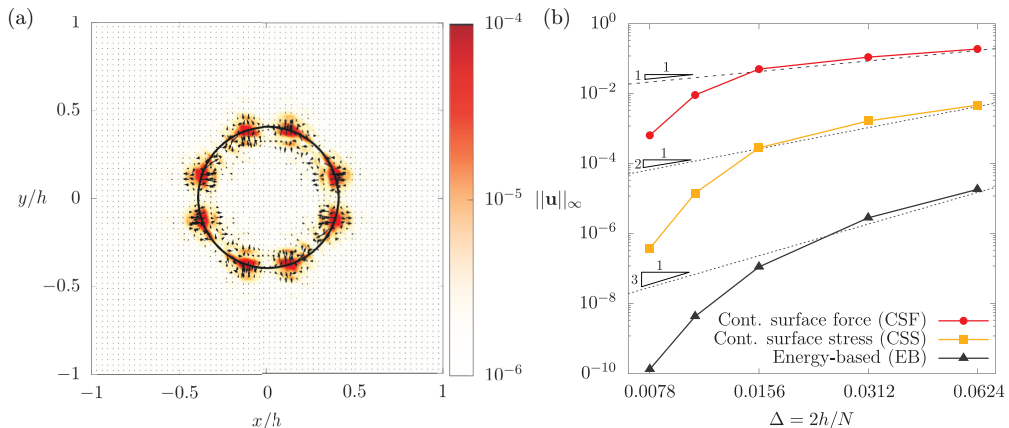


FIG. 4. Spurious currents observed in the benchmark simulation of a two-dimensional static drop immersed in quiescent fluid. The domain has dimensions $2h \times 2h$ and the drop diameter is $R/h = 0.4$ (with h the half-size of the domain, see the sketch of Fig. 3). The capillary width has been set equal to $\epsilon/h = 0.04$. The left panel shows the distribution of spurious currents in space, visualized by contour maps (red-high, white-low) of the L_∞ norm of the velocity field, $\|\mathbf{u}\|_\infty$. The interface position (isocontour $\phi = 0$) is shown with a black line and the flow field is represented using arrows. The case shown in panel a refers to the CSS approach for a grid spacing equal to $\Delta = 0.0312$ (corresponding to a grid resolution $N \times N = 64 \times 64$) Panel b shows the effects of different surface tension models and grid spacing $\Delta = 2h/N$ (where N is the number of grid points used) on the magnitude of the spurious currents. Results are generally better using the continuum-surface stress (CSS) or the energy-based (EB) approaches.

B. Modeling density and viscosity contrasts

Without loss of generality, we consider a two-phase flow, and we indicate as ρ_1 and ρ_2 the densities of the two phases, and η_1 and η_2 the corresponding viscosities (where subscripts 1 and 2 refer to dispersed and continuous phases, respectively). In the context of interface-resolved simulations, and more specifically of interface-capturing methods, density and viscosity are usually assumed to be proportional to the color function. This operation can be extended to phase-field methods by assuming that density and viscosity are linear functions of the phase-field variable [36,190,191]. An important advantage of using the phase-field ϕ as a basis function is that, being ϕ a smooth and continuous field, no additional operation is required to numerically discretize the density and viscosity maps. From a mathematical point of view, these maps are defined as

$$\rho(\phi) = \rho_1 \frac{(1 + \phi)}{2} + \rho_2 \frac{(1 - \phi)}{2}, \quad (19)$$

$$\eta(\phi) = \eta_1 \frac{(1 + \phi)}{2} + \eta_2 \frac{(1 - \phi)}{2}, \quad (20)$$

where $\phi = \pm 1$ are the phase-field values in the bulk of phases 1 and 2, respectively [192]. As previously mentioned, the implementation of these maps is straightforward as it does not require the computation of auxiliary smoothing kernels. Nevertheless, the use of Eqs. (19) and (20) in Navier-Stokes equations in conjunction with phase-field methods can lead to two issues. The first issue might arise when large density or viscosity ratios are considered: if the phase-field is not perfectly bounded between the bulk values (i.e., $\phi = \pm 1$ or $\phi = 0$ and 1, see Appendix A for details on this point) negative values of density or viscosity can be locally obtained. These unphysical values of density and/or viscosity can further amplify the problem of spurious currents, thus negatively influencing the stability and accuracy of the computation. To overcome this problem, two possible workarounds are available: (i) the first consists in clipping the phase-field values used to compute

the density and viscosity maps [124,193]; (ii) the second consists in using different interpolation kernels for the density and viscosity maps, as for instance kernels that rely on the harmonic mean rather than the classic arithmetic one [36,194,195].

The second issue is linked with the correct advection of mass and momentum in the Navier-Stokes equations. In particular, the presence of diffusive fluxes (or more in general sink/source terms) at the right-hand side of the phase-field governing equation displaces also mass when nonunitary density ratios are employed [96]. This issue, which is usually of secondary importance when low to moderate Reynolds numbers are considered [57,191,193,196,197], becomes particularly important when high Reynolds numbers and high-density ratios are considered. In this sense, modifications of the Navier-Stokes equations, so to make the phase advection consistent with the momentum advection, have been recently proposed: (i) changes of the momentum transport equation with the introduction of an auxiliary variable [198]; (ii) use of an entropy-viscosity method [199]; (iii) direct modifications of the momentum transport equation with the introduction of corrective terms [96,142,143,200,201].

IV. CAPABILITIES AND LIMITATIONS IN DESCRIPTION OF MULTIPHASE TURBULENCE

After having described the fundamental aspects of the phase-field modeling of multiphase turbulence, we discuss here the main capabilities and limitations of the phase-field approach. As shown in Fig. 1, the multiscale nature of multiphase turbulence imposes several challenges for numerical simulations. In particular, the desire of simulating each and every time and length scale has to face the limitations of computing power and available memory. The usual choice when interface-resolved simulation methods (e.g., phase-field methods) are employed is to avoid resolving the small interfacial scales and to resolve all turbulence scales: from the macroscopic problem scale, down to the Kolmogorov length scale. In this way, however, all phenomena occurring at scales smaller than this threshold are modeled or somehow smeared out. This choice has direct consequences on the description of topological changes of the interface, namely coalescence and breakage events. In the following, to assess the effects of modeling the smaller interfacial scales, the different stages composing a coalescence and a breakage event will be detailed. This description will be the starting point to discuss the main capabilities and limitations of the phase-field method.

A. Numerical description of topological changes of the interface

One of the most difficult tasks in the numerical prediction of drop-laden turbulent flows is the description of topological changes of the interfaces, namely the description of coalescence and breakup events. Let us consider a coalescence event, which can be divided into four stages [202]: (i) Approach: the two drops come closer and closer, and a thin liquid film is formed in between; (ii) film drainage: the thin liquid film between the drops starts to drain; (iii) film rupture: small-scale interactions lead to the rupture of the thin liquid film and to the formation of a coalescence bridge; (iv) reshaping: surface tension forces reshape the drop. Of the different stages mentioned above, film drainage and film rupture are governed by physical phenomena occurring at very small scales. In particular, during the final part of the film drainage, the thickness of the thin liquid film is about 10 to 100 nanometers [202–204]. Similar considerations hold for film rupture. Although a fundamental understanding of this stage is still lacking [202,205], during film rupture the main driving mechanisms are often assumed to be related to small-scale interactions as van der Waals attraction forces [206], thermal and capillary fluctuations [207–209], and overlap of diffusive interfacial layers [210]. The accurate simulation of these phenomena from first principles is highly desirable to accurately determine the outcome of the collision event: the interfaces might merge, leading to drop coalescence, or bounce off and separate. Unfortunately, such simulation is not possible and, while the numerical description of the approach and reshaping stages can be accurately described, the simulation of the film drainage and rupture stages is less accurate. This issue, which leads to as numerical coalescence, is typical of nearly all interface-capturing

methods, including the phase-field method (at least when interface-capturing methods are used in the single color/marker function formulation). Indeed, as the coalescence is implicitly handled by the method, two separate interfaces merge when they are closer than the grid spacing [211–214]. Thus, coalescence is influenced by the grid resolution, and the coalescence efficiency is often overestimated: standard interface-capturing methods have a unitary coalescence efficiency (meaning that all collisions result in a coalescence), while the actual measured coalescence efficiency is lower [215–217]. When energy-based phase-field methods are employed, this problem is also linked to two additional factors: (i) van der Waals attraction forces are not directly included, but they are modeled via the mixing energy term [218]; (ii) the use of realistic values of the capillary width in turbulent multiphase flow simulations is not possible and the interfacial layer has to be artificially enlarged.

To improve the description of coalescence, we can identify four possible approaches: (i) the coupling of molecular simulations to continuum simulations; (ii) the use of local or global mesh refinements; (iii) use of sub-grid models that account for effects that are not completely resolved; (iv) the use of multimarker phase-field formulation. The first possibility, coupling molecular dynamics simulations with continuum simulations, is in principle the most accurate and reliable solution [24,26,219]. However, this is usually difficult to implement, in particular when interface-interface interactions have to be accounted for. Indeed, the physical mechanisms underlying the rupture of the film are still unclear and are the object of ongoing investigations [202,205,220,221], and thus cannot be properly included in numerical simulations. In particular, different mechanisms at the core of the film rupture stage have been hypothesized: (i) small-scale interactions as van der Waals attraction forces [206]; (ii) thermal and capillary fluctuations [207–209]; (iii) overlap of diffusive interfacial layers [210]. An alternative solution is the use of dual grid resolution or adaptive mesh refinement schemes. In this way, simulations are still performed in the limit of the continuum, but the phase-field variable is computed on a more refined grid thus reducing the impact of numerical coalescence on the results. Although beneficial, this solution offers only a partial improvement in the simulation of coalescence events [25,222,223] since the actual scale at which coalescence occurs is still orders of magnitude smaller than the resolved one. The third possible approach is based on the inclusion of sub-grid models which try to mimic the unresolved small-scale physics [224,225]. This type of approach has been previously applied also to other interface-capturing [226–229] and interface-tracking methods [25,222,223]. For phase-field methods, seminal works in this sense date back to Körner *et al.* [230], who proposed a Lattice-Boltzmann-based phase-field method for the study of metallic foams [230,231]. A similar approach was followed by Benzi *et al.* [232] for densely packed systems to simulate the behavior of emulsions and foams [66,233]. The main idea is to introduce a term in the governing equations which accounts for the disjoining pressure that arises between two adjacent interfaces, which cannot be captured accurately by numerical simulations due to the limited available grid resolution [218]. Another possible strategy involves the use of multimarker phase-field method formulations [52,234,235]. The main idea behind this approach is to use a separate color function for each drop, similar to what has been previously done for other interface-capturing methods [229,236,237]. Within this framework, full control of the coalescence process is obtained: from situations in which coalescence occurs as in standard formulations, to situations in which it is tuned via ad-hoc models down to situations in which coalescence is completely forbidden. The naive implementation of this concept to simulate systems with a large number of drops is clearly not possible, for computational reasons (the computational cost would increase with the number of drops). However, the required number of marker functions (and the associated memory footprint) can be drastically optimized [234,236] thus making the use of this approach more attractive.

Let us now consider the dynamics of a breakage event, which can be divided into three stages [238,239]: (i) thread formation: the shear stresses stretch the drop, and a ligament is formed; (ii) pinch-off: the thread elongates and capillary instabilities pinch-off the ligament; (iii) thread breaking: the liquid thread breaks at the pinch-off section and the newly formed drops separate. Upon separation, surface tension reshapes the drops, and the threads are retracted. Overall, breakage

is a very quick phenomenon that can be well captured by the Navier-Stokes equations [211,240,241] without resolving the dynamics at the molecular scale. Hence, the description of breakages using Eulerian grids is considered to be rather accurate [242–244], although in the pinch-off region the high curvature of the interface might not be perfectly resolved. In this context, the phase-field method is very powerful as it allows for an implicit description of breakage events (being an interface-capturing method), and at the same time it allows for an accurate computation of the curvature and thus of the resulting surface tension forces. The description of breakage events can definitely be improved employing dual grids or adaptive mesh refinement approaches: the adoption of globally/locally refined grids improves the description of the dynamics at the pinch-off region, which is characterized by high curvature values and thus high surface tension forces. Although in most turbulent flows of interest, the Weber numbers evaluated using the integral scale of the system are large, the contribution of surface tension forces—and thus the desire to accurately represent them—is important when the dynamics of small drops (e.g., obtained from breakage of larger interfacial structures) is described. Indeed, for these small drops, the Weber number evaluated using local quantities (e.g., drop size) can be relatively small, thus suggesting an important role of surface tension forces [19].

B. Description of small interfacial structures

An additional issue arising from the limited resolution that one can reasonably afford when performing interface-resolved simulations is the minimum size of the interfacial structure that can be described. In particular, when the size of the drop becomes comparable to the grid size, the geometry of the interface is poorly defined, thus influencing curvature/surface tension forces calculation and mass conservation. In fact, for phase-field methods, the issue of describing small interfacial structures mainly influences mass conservation. As the transition layer is always numerically resolved with a few grid points, curvature and surface tension forces are in general well represented, even when small drops are described. Strategies aimed at improving the description of small interfacial structures usually rely—similarly to what happens for breakage events—on dual grid resolution or adaptive mesh refinement schemes. An alternative solution, however not yet employed in phase-field methods, is the adoption of hybrid Eulerian-Lagrangian formulations [245–251]: A drop is described by an Eulerian approach as long as its size is larger than a certain threshold (usually, about few grid cells), while it starts to be described by a Lagrangian pointwise approach when its size becomes smaller than the prescribed threshold.

In the context of phase-field methods, the description of small interfacial structures is also influenced by the shrinkage phenomenon [104]. This phenomenon can be traced back to the thermodynamic background present in the governing equations. In particular, a reduction of the free energy of the system can be obtained by shifting the bulk values of the phase-field variable and at the same time shrinking the drop/bubble [104]. This is a direct consequence of the attained equilibrium profile: this profile represents the exact solution for a planar interface, but not for a curved interface [126]. The impact of the shrinkage on simulation results depends on the employed phase-field formulation: phase-field methods that are based on the standard Cahn-Hilliard equation or use time-dependent Lagrangian multipliers in conjunction with the Allen-Cahn equation are expected to be more influenced by this problem. Nevertheless, even when these formulations are employed, the problem can be largely mitigated by a proper setting of the parameters [104].

C. Capabilities and limitations in the description of drop-laden turbulent flows

In the following, we will summarize capabilities and limitations of the phase-field method to describing drop-laden turbulent flows. The main limitation, which is shared to some extent with other interface-tracking and capturing methods, comes from the limited resolution one can reasonably afford, and thus reflects into the impossibility to resolve all the small but potentially significant scales of the system [7,25,222,243], from the large integral scale of the system down

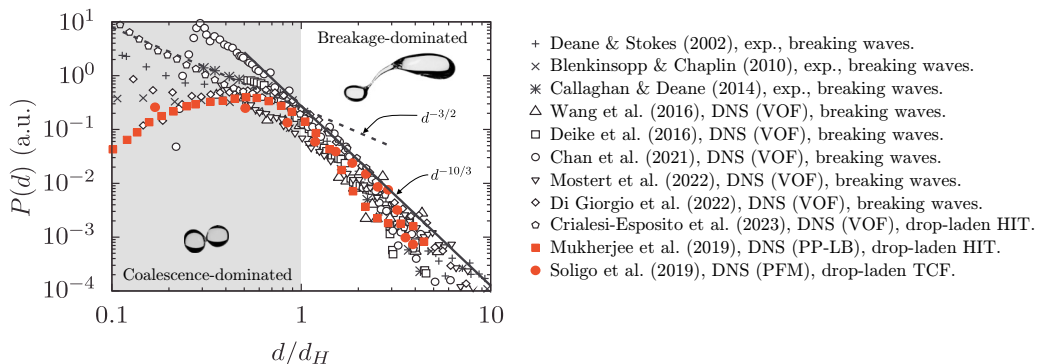


FIG. 5. Comparison of size distributions obtained from experimental and numerical investigations of breaking waves and drop-laden turbulent flows [homogeneous isotropic turbulence (HIT) and turbulent channel flow (TCF)]. The drop diameter is normalized using the Kolmogorov-Hinze scale for each case (estimated when not enough information is provided) while the distributions are reported in arbitrary units due to the different normalizations used. Data is taken from: Deane and Stokes [254] (field observations on breaking waves), Blenkinsopp and Chaplin [255] (field observations on breaking waves), Callaghan *et al.* [256] (experiments on breaking waves), Wang *et al.* [257] (breaking waves DNS-VOF, time average), Deike *et al.* [258] (breaking waves DNS-VOF, time average), Chan *et al.* [264] (breaking waves DNS-VOF, time average), Mostert *et al.* [259] (breaking waves DNS-VOF, higher Reynolds number case), Di Giorgio *et al.* [4] (breaking waves DNS-VOF, higher Reynolds number case), Crialesi-Esposito *et al.* [253] (drops in homogeneous isotropic turbulence, DNS-VOF, 10% volume fraction), Mukherjee *et al.* [65] (drops in homogeneous isotropic turbulence, DNS-LBM, case P2), and Soligo *et al.* [211] (surfactant-laden drops in turbulent channel flow, higher surfactant strength case). The analytic scaling laws for the coalescence- and breakage-dominated regimes, $d^{-3/2}$ and $d^{-10/3}$, are also reported as a reference. A good agreement is obtained in the breakage-dominated regime, i.e., for drops larger than the Kolmogorov-Hinze scale.

to the molecular scales (which, as already mentioned, control the dynamics of film rupture and thus the outcome of drop-drop/bubble-bubble interactions, i.e., bouncing, sliding or coalescence). This limitation is expected to influence mainly the interaction between small drops—in the limit of low dispersed phase volume fractions—or densely packed systems like emulsions and foams—in the limit of high dispersed phase volume fractions—where interface-interface interactions are the main ingredient that controls the system topology and thus its behavior (e.g., effective viscosity, size distribution). For the low volume fraction regime, which is the principal focus of this review, the limitations on the grid resolution can have an influence on the results obtained in coalescence-dominated conditions, typical of microsystems in laminar conditions. However, the limitation on the grid resolution can be considered of secondary importance when the system is governed by large-scale dynamics, as it occurs in turbulent flows where energy is transferred from the larger integral scales down to the dissipative Kolmogorov scale. In this case, the dynamics of drops is dominated by breakages, which are not much influenced by the unresolved molecular scales behavior [25,222,223,243], and can be predicted accurately.

These considerations are confirmed by the comparison between the drop size distributions obtained from phase-field simulations and those obtained from other simulation techniques and experimental data, Fig. 5. In particular, we compare the drop size distributions obtained from phase-field simulations [252] [65,211] of drop-laden turbulent flows (homogeneous isotropic turbulence, HIT, and turbulent channel flow, TCF) against those obtained from VOF simulations of drop-laden homogeneous isotropic turbulence [253] and experimental (exp.) of numerical (DNS) investigations of breaking waves [4,254–259]. The analytical scaling laws [260], $d^{-3/2}$ and $d^{-10/3}$, for the coalescence- and breakage-dominated regimes are also reported as reference. Analyzing Fig. 5,

we can observe the emergence of two regimes depending on the Kolmogorov-Hinze (KH) scale, d_H , which identifies the critical diameter below which a drop/bubble will not undergo breakage according to the KH framework [261,262]. For drops/bubbles smaller than the Kolmogorov-Hinze scale, we observe the coalescence-dominated regime (left side of Fig. 5). In this regime, drops are unlikely to break, as they are smaller than the critical scale; instead, they are more prone to change their size by coalescence with other drops. For drops/bubbles larger than the Kolmogorov-Hinze scale, we have the breakage-dominated regime, where the main mechanism by which drops change their size is breakage. For the coalescence-dominated regime, it is difficult to infer the correct trend as the different types of data (experimental, numerical, and analytical) are quite scattered. For very small diameters, we can observe a deviation between phase-field simulation results and the analytical scaling law. This can be traced back to two main reasons: (i) coalescence efficiency is overestimated in interface-capturing simulations; (ii) using Eulerian methods, the grid resolution limits the smallest drop/bubble that can be accurately resolved. In addition, it must be also noted that due to the grid requirements imposed by DNS, the scale separation between the Kolmogorov-Hinze scale and the dissipative Kolmogorov scale is at best about one order of magnitude for the most recent simulations. This limits the range of scales in which the coalescence-dominated regime can be observed. Moving to the breakage-dominated regime, we note a good agreement between phase-field results, experimental data, analytical scaling laws, and numerical data obtained with different methods. This highlights the capabilities of PFM-based simulations, and more in general of interface-resolved simulation methods, to accurately describe breakage events. Finally, it is interesting to observe that, despite the different flow configurations considered here (breaking waves, HIT, TCF), a good agreement is obtained among the different studies, suggesting that the idea of a turbulent break-up cascade can be applied with reasonable accuracy to most of the drop- and bubble-laden turbulent flows [263,264].

V. BEYOND MULTIPHASE TURBULENCE: HEAT AND MASS TRANSFER

So far, we have discussed the capabilities of phase-field modeling in describing drop- and bubble-laden flows. Multiphase turbulence is however not limited to systems composed of two pure phases. Indeed, the transport of heat and mass in dispersed multiphase systems is the hallmark of many industrial and natural phenomena: from vaporization of atomized fuel jets [19,265] in combustion engines, to rain formation and atmosphere-ocean heat/mass exchanges [3,266]. Due to the relevance of the problem, different techniques have been developed for the investigation of heat and mass transfer in two-phase systems. These developments have been mostly focused on front-tracking [267–269], volume-of-fluid [265,270–272], level-set [273,274], and Lattice-Boltzmann methods [87,275–279]. Possible approaches for phase-field methods have been proposed only recently [82,84,85,88].

The accurate description of heat and mass transfer phenomena in multiphase flows poses additional challenges. In particular, even for the one-way coupling regime, in which the volume changes associated to the heat/mass transfer are neglected, numerical schemes able to provide an accurate evaluation of the interfacial heat and mass flux or to describe the surfactant concentration are required. When the hypothesis of negligible volume changes produced by the mass transfer process is lifted (two-way coupling regime), as common in evaporation and boiling processes, an additional challenge arises: methodologies able to handle discontinuous and nonsolenoidal velocity field, as well as to incorporate compressibility effects, are required. In addition, it must be also pointed out that, for the case of practical interest, the relevant scales of the temperature/mass fraction field (i.e., the Batchelor scale [280,281]) are smaller than the Kolmogorov scale, thus enforcing a further restriction on the grid resolution. In the following, the challenges and the methodologies available for the description of heat and mass transfer phenomena will be discussed. We will start by considering the transport of surfactants and thermocapillary effects, and then move to heat and mass transfer processes in the one- and two-way coupling regimes.

A. Surface Tension gradients due to surfactants or thermocapillary effects

Surfactants are molecules that naturally collect at the interface between two fluids, thus modifying the cohesive forces among fluid molecules and the surface tension value [282]. Their distribution at the interface, which is in general not uniform, makes the interfacial dynamics more complex to predict: not only the magnitude of capillary forces is reduced by the presence of surfactants, but also the gradients of surfactants concentration along the interface generate Marangoni forces [283–285], which act tangentially to the interface. Due to their importance in many industrial and environmental flow instances [286–289], modeling and simulation of surfactant-laden flows receive ever-increasing attention. The choice of the numerical approach used to describe surfactants depends on the type of surfactant considered (nonionic, anionic, cationic, amphoteric, etc.), system configuration (liquid/liquid or gas/liquid), and fluid properties (polar or nonpolar, etc.). Generally speaking, we can categorize surfactants into two categories: soluble and insoluble surfactants [290]. Surfactants do not dissolve in gases and their solubility in liquids depends on the surfactant and liquid chemical properties [282,290]. Thus, based on the case considered, surfactants exhibit different dynamics: soluble surfactants can move along the interface and can absorb/desorb in the bulk of the phase while insoluble surfactants are limited only to the transport over the interface. The different characteristics of surfactants are reflected in the approaches used to track the surfactant concentration in numerical simulations [7]. For insoluble surfactants, a transport equation [291] is resolved on the interface or, for numerical reasons, in a narrow band about the interface. For soluble surfactants, two possible approaches are available: i) the single equation model [80,292,293], in which one equation is used in the entire domain; ii) the multiple equations models [294,295], in which two or more equations, coupled at the interface, are used to describe interfacial and bulk dynamics.

Several approaches for the description of insoluble and soluble surfactants (using single or multiple equations models) are available for front-tracking [267,294,295], volume-of-fluid [296,297], and level-set methods [274,298–300]. In the context of phase-field methods, soluble surfactants tracked using single equation models is the most common approach [80,292,293]. Specifically, soluble surfactants can be straightforwardly described by introducing, in addition to the phase-field ϕ , another order parameter that represents the surfactant concentration, ψ . Additional terms (which depend on the surfactant concentration) are also included in the Ginzburg-Landau free energy functional. These terms can account for different aspects of the surfactant dynamics [80,292,293,301–303]: (i) preferential accumulation of surfactant molecules at the interface; (ii) entropy reduction obtained when the surfactant is homogeneously distributed in the bulk of the phases; (iii) lateral interaction between molecules (e.g., saturation effects); (iv) different solubilities in the bulk of the two phases; (v) other effects. The surfactant concentration is governed by a Cahn-Hilliard-like equation:

$$\frac{\partial \psi}{\partial t} + \mathbf{u} \cdot \nabla \psi = \nabla \cdot (\mathcal{M}_\psi \nabla \mu_\psi), \quad (21)$$

where \mathcal{M}_ψ represents the surfactant mobility (which can be set as constant or variable) and μ_ψ is the surfactant chemical potential, which similarly to the phase-field chemical potential, can be obtained as the functional derivative of the Ginzburg-Landau free-energy (with respect to the surfactant concentration):

$$\mu_\psi = \frac{\delta \mathcal{F}[\phi, \nabla \phi, \psi]}{\delta \psi}. \quad (22)$$

The resulting order of the Cahn-Hilliard-like for the surfactant depends on the nature of the additional terms included in the Ginzburg-Landau free energy functional [304]. When logarithmic terms are employed [301,302], the mobility is usually defined as variable so that a diffusive term is obtained and the governing equation is of second order. In contrast, when squared gradients terms are employed [81,304,305], the mobility is commonly set as constant, and a fourth-order equation is obtained.

Surfactants can have different solubility not only in gas/liquid flows (for example air and water), but also in liquid/liquid flows (for example in flows with water and oil, see [306]), making the

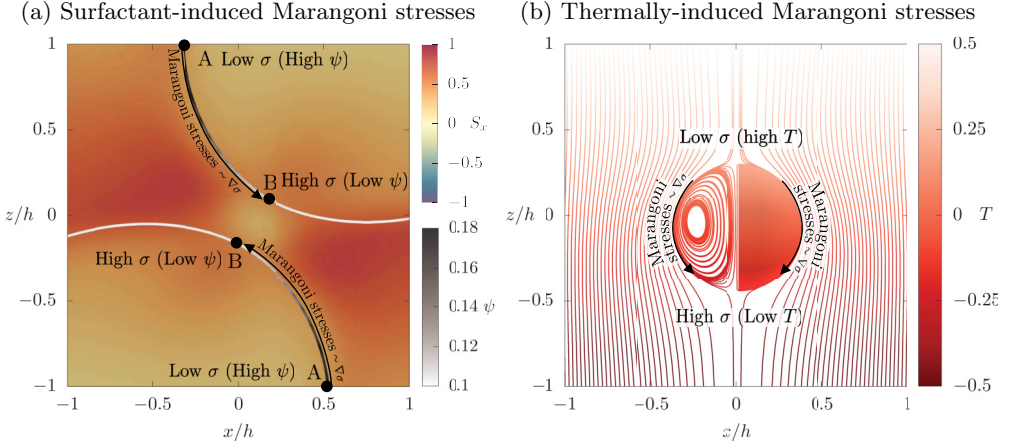


FIG. 6. Development of Marangoni stresses in two different flow instances: interaction between surfactant-laden droplets in shear flow (a), and migration of a droplet in a still fluid with top-down heating (b). In panel (a), two surfactant-laden droplets collide in shear flow. The difference in surfactant concentration ψ (white-low; black-high) between points A and B, generates a surface tension gradient and thus Marangoni stresses (directed from point A to B). These stresses slow down the drainage of the thin liquid film and thus hinder drop coalescence. Contour maps represent the value of the strain rate $S_x = (\partial u/\partial z + \partial w/\partial x)/2$. The reader is referred to Soligo *et al.* [83] for details. In panel (b), the migration of a droplet in a still fluid with a vertical temperature gradient (top-down heating) is shown [307]. The temperature difference between the upper part (high temperature) and the bottom part (low temperature) of the droplet generates a surface tension gradient and thus Marangoni stresses. These stresses produce the upward migration of the droplet.

study of surfactants with different solubility very important in many different applications. In the context of the phase-field method, this can be easily handled by introducing a skewed term in the free energy functional, so to penalize the presence of the surfactant in one of the two phases. In this case, the free energy functional $\mathcal{F}[\phi, \nabla\phi, \psi]$ usually employed for surfactant-laden drops [83] is completed by a term that reflects and models the unequal solubility of the surfactant

$$f_{ax}(\psi, \phi) = e\psi\phi, \quad (23)$$

where e is a parameter that controls the bulk concentration of the surfactant in the penalized phase [303].

As already anticipated, surface tension not only depends on the presence of surfactants, as discussed above, but might depend also on other factors, for example, electric and magnetic fields or temperature [308,309]. Of specific practical and historical importance is the dependence of surface tension on temperature. In many applications, a linear dependence of σ on temperature T can be assumed [310]:

$$\sigma(T) = \sigma_0 - \beta_T(T - T_0), \quad (24)$$

where σ_0 is the value of the surface tension at the reference temperature T_0 , while β_T is the surface tension coefficient, i.e., $\beta_T = -\partial\sigma/\partial T|_{T=T_0}$. When the surface temperature is not uniform, surface tension gradients

$$\nabla_s\sigma = -\beta_T(\mathbf{I} - \mathbf{n} \otimes \mathbf{n}) \cdot \nabla T, \quad (25)$$

exist and induce, very much like surfactants do, Marangoni stresses that act tangentially to the interface. The action of Marangoni stresses is depicted in Fig. 6 for two different flow instances: (i) interaction between two surfactant-laden droplets [Fig. 6(a)]; (ii) thermocapillary migration of a droplet [Fig. 6(b)]. In the first case [Fig. 6(a)], Marangoni stresses drive fluid from low surface

tension regions (high surfactant concentrations, black region at the drop interface, point A) to high surface tension regions (low surfactant concentration, white region at the drop interface, point B). In this case, Marangoni stresses hinder the drainage of the thin liquid film, thus avoiding drop coalescence [284,287,311] (or at least delaying it). In the second case [Fig. 6(b)], a drop is immersed in still fluid with top-down heating [307]. As a consequence, warmer regions at the top of the drop surface will be characterized by smaller values of surface tension, while colder regions at the bottom of the drop surface will be characterized by larger values of surface tension. This induces Marangoni stresses in the direction of the surface tension gradient (i.e., from regions of low surface tension, and higher temperature, to regions of high surface tension, and lower temperature). It is the so-called thermocapillary effect [283,312]. The thermocapillary effect is observed in various situations and has applications in different fields, including heat transfer in microgravity conditions, melting and solidification patterns in material processing, film coating, and of course bubble and droplet dynamics [309,313–315]. However, albeit extensively studied in laminar conditions, thermocapillary effects are almost unexplored in turbulence, and may represent a fertile field of research for the future.

B. Heat and mass transfer (one-way coupling regime)

We consider now the heat and mass transport when the associated volume change is neglected, i.e., in the limit of small concentrations or small density effects. This implies that the heat and mass transport does not have a feedback on the momentum and mass conservation equations, if we exclude small density variations whose effect can be accounted for using the Boussinesq approximation. To understand the challenges associated with the description of heat and mass transfer in this regime, we briefly recall the physical mechanisms driving heat/mass transfer. For heat transfer, the main driving mechanism is thermal equilibrium. At the interface, the temperature is continuous and the following heat balance applies:

$$T_1 = T_2; \quad k_1(\nabla T_1 \cdot \mathbf{n}) = k_2(\nabla T_2 \cdot \mathbf{n}), \quad (26)$$

where T_1 and T_2 are the temperatures of the two phases and k_1 and k_2 the corresponding thermal conductivities. Differently, the specific heat content, defined as $q_i = \rho_i C_{p,i} T_i$, exhibits a jump across the interface:

$$\frac{q_1}{q_2} = \frac{\rho_1 C_{p,1}}{\rho_2 C_{p,2}} = H_q, \quad (27)$$

where H_q is the equivalent of the Henry coefficient for heat transfer. For mass transfer, the main driving mechanism is the difference in chemical potentials. At the interface, chemical potentials can be considered continuous; note that this is an approximation that holds as far as the flow is far from sonic conditions [316,317]. Hence, this condition together with the mass balance equation at the interface gives

$$\mu_1 = \mu_2; \quad D_1(\nabla c_1 \cdot \mathbf{n}) = D_2(\nabla c_2 \cdot \mathbf{n}), \quad (28)$$

where μ_1 and μ_2 are the chemical potentials of the two phases, D_1 and D_2 the mass diffusivities and c_1 and c_2 the volumetric concentrations. The volumetric concentrations exhibit a jump across the interface that is determined by the Henry law (obtained from chemical potential equilibrium):

$$\frac{c_1}{c_2} = H_c, \quad (29)$$

where H_c is the Henry coefficient.

From the above discussion, we can appreciate the similarity between heat and mass transfer, as summarized in Fig. 7. For this reason, numerical techniques for heat or mass transfer are usually developed referring to a generic variable θ , which can be either a conserved quantity (specific heat content or volumetric concentration) or a continuous quantity (temperature or chemical potential).

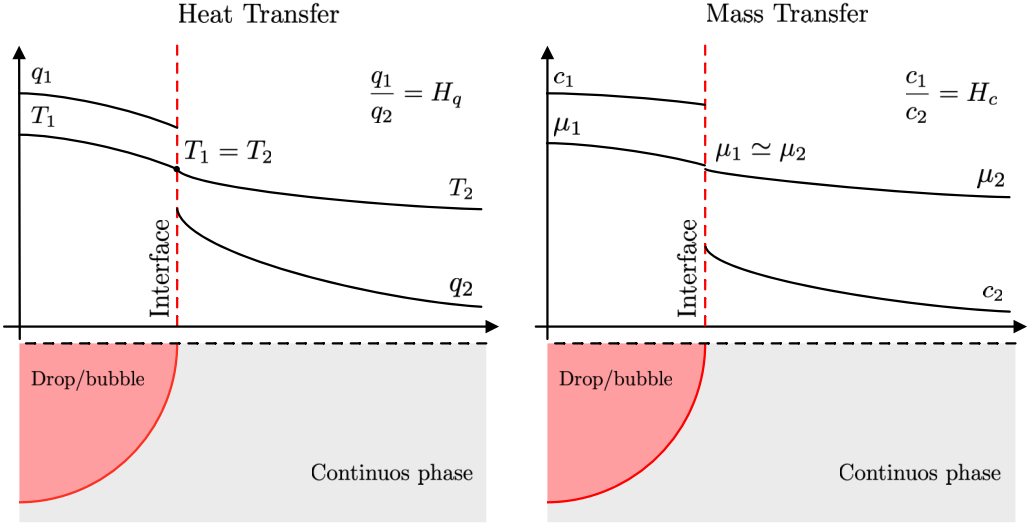


FIG. 7. Duality between heat and mass transfer processes in the one-way coupling regime. The two plots show the behavior of the specific heat content q_i , temperature T_i , chemical potential μ_i , and volumetric concentration c_i along the dashed line of the sketch reported below each plot. For heat transfer, the temperature is continuous at the interface, while the specific heat content exhibits a jump at the interface. For mass transfer, chemical potentials can be approximated as continuous, while the volumetric concentrations exhibit a jump at the interface.

The models available in literature for heat and mass transfer problems can be classified into two categories: one-scalar and two-scalar models [85,318,319].

One-scalar models rely on a single equation that is solved in the entire domain to describe the heat and mass transfer in a one-fluid fashion:

$$\frac{\partial \theta}{\partial t} + \nabla \cdot (\mathbf{u}\theta) = \nabla \cdot \left[D(\phi) \nabla \left(\frac{\theta}{H(\phi)} \right) \right] + f_c, \quad (30)$$

where $D(\phi)$ represents the effective diffusivity and $H(\phi)$ the effective ratio (used to remove the interfacial jump), and are usually evaluated as a function of the phase field [84,319], while f_c is an additional flux that can be used to enforce transport consistency [319]. This approach, which has been used in the context of volume-of-fluid [270,320,321], level-set [322–324], and phase-field methods [84,85,319,325,326], provides an accurate estimate of the heat or mass transfer only when the discontinuity in the field obtained at the interface is advected exactly as the interface boundary [317]. Satisfying this requirement becomes difficult when the ratio between the two diffusivities or the interfacial jump becomes larger (e.g., gas/liquid systems) and artificial mass leakage is observed [85,319].

To avoid this issue, two-scalar models can be employed. These models rely on two scalar equations, one for each phase, to describe the heat or mass transfer. This approach has previously applied to volume-of-fluid methods [316,317,327,328] and recently extended to phase-field methods [85,318,319]. The resulting set of equations is [329]

$$\frac{\partial \theta_1}{\partial t} + \nabla \cdot (\mathbf{u}\theta_1) = \nabla \cdot \left[D_1 \left(\nabla \theta_1 - \frac{\sqrt{2}(1-\phi)}{\epsilon} \mathbf{n}\theta_1 \right) \right] + S, \quad (31)$$

$$\frac{\partial \theta_2}{\partial t} + \nabla \cdot (\mathbf{u}\theta_2) = \nabla \cdot \left[D_2 \left(\nabla \theta_2 + \frac{\sqrt{2}(1+\phi)}{\epsilon} \mathbf{n}\theta_2 \right) \right] - S, \quad (32)$$

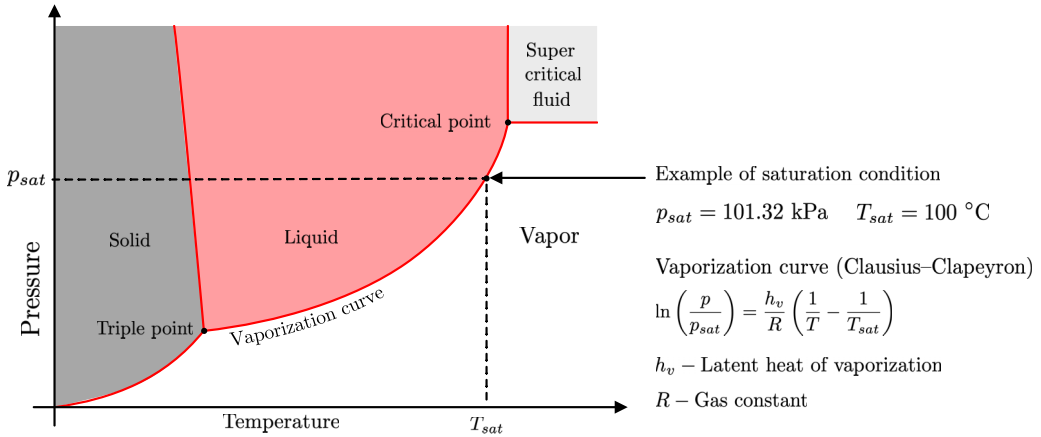


FIG. 8. Sketch of the thermodynamic pressure-temperature diagram for water. Two important points can be identified: the triple point (bottom left) where solid, liquid, and vapor coexist and the critical point (right top), the last thermodynamic state at which liquid and vapor coexist. For liquid/vapor transformations, the reference curve is the vaporization curve that defines the saturation condition as a function of pressure and temperature, and whose behavior can be inferred from the Clausius-Clapeyron equation.

where \mathbf{n} is the interface normal vector and S are closure terms, here reported in a compact form and whose complete definition can be found in Mirjalili *et al.* [85]. The resulting scalar concentration in the domain can be obtained as $\theta = \theta_1 + \theta_2$. The proposed two-scalar model exhibits accurate results in terms of both heat and mass transfer predictions and can be also extended to the degenerate case in which one phase has zero diffusivity [330].

C. Heat and mass transfer (two-way coupling regime)

When the hypothesis of negligible volume change is removed, heat, mass, and momentum transfers mutually interact. The two most important flow instances of this kind are evaporation and boiling processes, and we restrict here to these for the sake of brevity. To appreciate the challenge associated with the numerical description of evaporation and boiling, it is worth briefly recalling the physical mechanisms governing these processes. We start by considering the thermodynamic pressure-temperature diagram for water reported in Fig. 8. We can identify two important points: the triple point (bottom left), in which the solid, liquid, and gas coexist, and the critical point (top right), the last thermodynamic condition at which liquid and gas can coexist. These points are connected by the so-called vaporization line; this line defines the saturation condition as a function of pressure and temperature and can be inferred from the Clausius-Clapeyron relation. For a given pressure, using this diagram, we can discriminate between evaporation and boiling: the former occurs at temperatures lower than the saturation condition (obtained from the vaporization curve) while the latter occurs at temperatures equal to or larger than the saturation temperature. The physical mechanisms leading to evaporation and boiling are therefore different: evaporation occurs only at the liquid/gas interface, and is due to the motion of molecules with high enough energy to leave the liquid interface [331]; boiling occurs in the entire bulk of the liquid with the nucleation of vapor bubbles. For this reason, boiling is generally a much more complex phenomenon, characterized by different regimes and configurations (e.g., pool boiling, flow boiling).

In case of evaporation and boiling, the interfacial boundary conditions (jump conditions) are modified to accommodate the resulting volume change [332], Fig. 9. For the velocity field, using

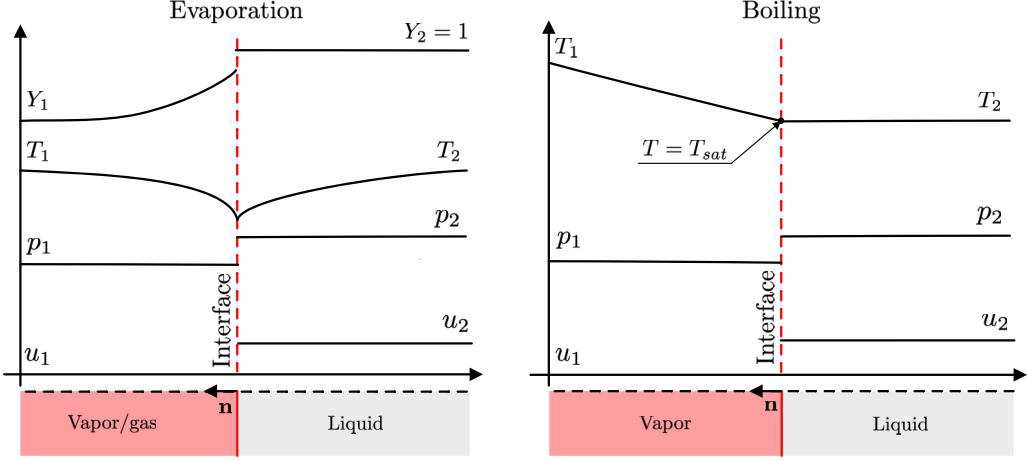


FIG. 9. Sketch of the jump conditions at the gas/vapor-liquid interface for evaporation (left) and boiling (right). The configuration resembles the Stefan problem, where the left boundary is a wall and the right is a free outlet (see sketch). During the evaporation/boiling process, the interface advances from left to right. The qualitative behavior of velocity, pressure, temperature, and vapor mass fraction (for evaporation) is also reported. The main difference between evaporation and boiling can be also appreciated: for evaporation, the interface is not always in saturation condition, while for boiling saturation conditions are found at the interface and in the bulk of the liquid.

the Rankine-Hugoniot condition we obtain

$$\mathbf{u}_1 \cdot \mathbf{n} = \mathbf{u}_2 \cdot \mathbf{n} + \dot{m} \left(\frac{1}{\rho_1} - \frac{1}{\rho_2} \right), \quad (33)$$

where subscript 1 identifies the vapor/gas and 2 the liquid, \dot{m} is the mass flux (positive for evaporation/boiling and negative for condensation) and \mathbf{n} is the interface normal vector. For the pressure, we have

$$p_1 = p_2 - \sigma \kappa + 2[\mu_1 \mathbf{n}^T \cdot \nabla \mathbf{u}_1 \cdot \mathbf{n} - \mu_2 \mathbf{n}^T \cdot \nabla \mathbf{u}_2 \cdot \mathbf{n}] - \dot{m}^2 \left(\frac{1}{\rho_1} - \frac{1}{\rho_2} \right), \quad (34)$$

where the first term accounts for surface tension forces [333] and the other two terms account for the different viscosity of the two phases, and for the Stefan flow generated by evaporation/boiling. It is worth observing that these jump conditions do not depend on the mass transfer mechanism considered. The mechanism, instead, influences the jump conditions on the transport of energy and mass fraction. For evaporation, the transport of energy and of vapor fraction must be solved, subject to the following jump condition for the temperature field at the interface:

$$k_1(\nabla T_1 \cdot \mathbf{n}) = k_2(\nabla T_2 \cdot \mathbf{n}) + \dot{m}[h_v + (C_{p,1} - C_{p,2})(T_i - T_{\text{sat}})], \quad (35)$$

where h_v is the latent heat of vaporization, T_i and T_{sat} the interface and saturation temperatures, and the following condition the vapor mass fraction

$$\rho_1 D_1 \nabla Y_1 \cdot \mathbf{n} = \rho_2 D_2 \nabla Y_2 \cdot \mathbf{n} - \dot{m}(Y_1 - Y_2) = \dot{m}(1 - Y_1), \quad (36)$$

where the last simplification is valid for a single-component liquid ($Y_2 = 1$ and $\nabla Y_2 = \mathbf{0}$). For boiling, pure liquid and vapor systems are usually considered, and only the energy equation is solved assuming saturation condition at the interface $T_i = T_{\text{sat}}$. Thus, the jump condition (35) simplifies as

$$k_1(\nabla T_1 \cdot \mathbf{n}) = k_2(\nabla T_2 \cdot \mathbf{n}) + \dot{m}h_v. \quad (37)$$

The mass flux \dot{m} can be computed from equation (36) valid for evaporation:

$$\dot{m} = \frac{\rho_1 D_1 \nabla Y_1 \cdot \mathbf{n}}{1 - Y_1}, \quad (38)$$

and from Eq. (37) valid for boiling

$$\dot{m} = \frac{(k_1 \nabla T_1 - k_2 \nabla T_2) \cdot \mathbf{n}}{h_v}, \quad (39)$$

other closure relations for the mass flux evaluation can be found in Kharangate and Mudawar [334].

The analysis of the jump conditions gives a complete overview of the challenges associated with the description of evaporation and boiling phenomena. In addition to the evaluation of the interface shape and its topological changes, and to the description of concentration/temperature fields in systems that can have very different thermophysical properties, the accurate numerical description of phase change requires methods that can handle a discontinuous and nonsolenoidal velocity field, possibly incorporating also effects of compressibility in the vapor/gas phase.

The first seminal works in this context were based either on the front-tracking [335] or volume-of-fluid methods [336]. Improvements to the original methods were later developed [269,272,337], and also proposed for other interface-capturing methods, like the level-set methods [338–341] (see Rajkotwala *et al.* [342] and Kharangate and Mudawar [334] for reviews on the topic) even for the case of turbulent flows [343,344]. The above-mentioned works rely on a one-fluid formulation, in which proper extensions of the velocity fields into the vapor/liquid phase are used to account for the velocity jump that arises at the interface. Alternatively, ghost-fluid methods, which are generally combined with a level-set-based representation of the interface, have been also employed [273,338,339,345]: thanks to the possibility of directly imposing jump conditions on the velocity/pressure field using ghost nodes, this class of methods represents an attractive option for flows with discontinuous velocity fields.

Recently, phase-field methods have been developed to describe evaporation and boiling phenomena. In particular, methodologies based on the Cahn-Hilliard equations [88] or the Allen-Cahn equations [86,346] have been proposed and have shown promising results. Lattice-Boltzmann phase-field methods have also proved to be a viable approach for the description of phase-change phenomena, either using an approximation of the Cahn-Hilliard or Allen-Cahn equation [87,276–279].

VI. FUTURE PERSPECTIVES AND CONCLUSIONS

In this paper, we have discussed the main capabilities and limitations of phase-field methods in describing drop-laden turbulent flows, and we have outlined the challenges associated with the description of more complex flows, i.e., when heat and mass transfer phenomena are also present. The phase-field method, coupled with direct numerical simulation of the Navier-Stokes equations, represents a powerful tool capable of accurately describing the dynamics of dispersed multiphase flow. This method, because of its Eulerian nature, is capable of accurately describing arbitrary interface shape and deformation as well as its topological changes (e.g., coalescence and breakage) without the need for additional algorithms for geometrical reconstruction or topology handling. This favors the development and use of fast, efficient, and scalable parallel solvers, which can be used to readily solve the governing equations [197], and makes the phase-field method particularly suited for large-scale simulations of drop-laden turbulent flows in cutting-edge HPC infrastructures. In addition, as different phase-field formulations are available, from fourth-order formulations based on the Cahn-Hilliard equation to second-order formulations based on the Allen-Cahn equation, a vast number of numerical techniques can be employed.

Considering the description of multiphase turbulence, the phase-field method allows for an accurate description of the flow field: As the phase variable is a smooth field, curvature, surface tension forces, and the corresponding exchanges of momentum can be accurately described without the need

for additional kernels or interpolation operations. Moving to the description of topological changes of the interface, the method well describes breakage events, as confirmed by the size distributions obtained in the breakage-dominated regime when compared to archival experimental [254–256], numerical [4,253,257–259,264], and analytical [260] data. Similarly to nearly all interface-capturing methods, predictions of coalescence events is less accurate, because of the unresolved small-scale physics which happens beyond the grid resolution limits. Local or global grid refinements—dual grid resolution schemes [58,117] or automatic mesh refinement techniques [118–122,347]—can be used to improve the description of coalescence, although their use is not completely resolute. Further improvements in this sense can be achieved using multimarker formulations, coalescence models, and combination thereof [226–229]. While these approaches have been applied in the past to other interface-capturing techniques showing promising results, their use in the context of phase-field methods is an almost unexplored field of research and only recently multimarker phase-field formulations have been tested [52,234]. Finally, considering the description of small interfacial structures, improvements in this sense can be obtained by employing dual grid resolution schemes or automatic mesh refinement techniques. More involved techniques, for instance, the use of hybrid Eulerian-Lagrangian approaches [245–251], have not been well explored and represent a possible way for future developments.

Going beyond isothermal multiphase turbulence, and moving to systems where also heat and mass transport processes take place, capabilities of phase-field methods have not been fully tested yet. Specifically, while for the description of surfactant-laden interfaces, a considerable number of works that employ the phase-field method is available in archival literature [80,292,293,301–303] (thanks also to the straightforward implementation of surfactant description in phase-field methods), the number of works in which heat and mass transfer is accounted for is much more limited. This is due to the additional numerical challenges associated with the description of heat and mass transfer. Indeed, in most cases of practical interest, two additional issues arise: (i) the properties of the two phases (e.g., thermal and mass diffusivities) are very different, thus requiring the use of proper schemes to avoid artificial heat/mass leakage [85,319]; (ii) the relevant scales of the temperature/mass fraction field (i.e., the Batchelor scale [280,281]) become smaller than the Kolmogorov scale, thus posing further restrictions on the grid requirements. When phase change phenomena are considered (two-way coupling regime), the nondivergence flow field obtained at the interface poses a further challenge, thus requiring proper modifications of the flow solver [86–88,276–279,346]. Overall, despite the current number of works that employ the phase field for the description of heat and mass transfer is limited, the number of contributions in this sector is expected to grow in the future.

ACKNOWLEDGMENTS

We acknowledge CINECA, PRACE, EURO HPC JU, and VSC for awarding us access to Tier-0 and Tier-1 machines through national and European call, among which Fermi@CINECA, Marconi-KNL@CINECA, Marconi-100@CINECA, Leonardo@CINECA, LUMI-C@LUMI, HAWK@HLRS, Joliot-Curie@KNL, Discoverer@Sofiatech, VSC-3, VSC-4, and VSC-5@VSC. We also gratefully acknowledge financial support from the MSCA-ITN-EID project COMETE (Project No. 813948) and the PRIN project Advanced Computations and Experiments for anisotropic particle transport in turbulent flows (ACE). The authors thank Luc Deike, Marco Cialesi Esposito, and Simone Di Giorgio for the supporting information and data on bubble statistics.

APPENDIX A: CONSERVATION OF TOTAL MASS AND INDIVIDUAL PHASE MASS

The use of governing equations that satisfies the global mass conservation constraint combined with the employment of a conservative numerical method leads to the mathematical and numerical

conservation of the phase-field variable over time; in mathematical terms:

$$\frac{\partial}{\partial t} \int \phi d\Omega = 0, \quad (\text{A1})$$

where Ω is the computational domain considered. Equation (A1) enforces the global mass conservation of the entire system; however, it does not guarantee the conservation of the mass of each individual phase, i.e., the mass enclosed by the interface [104,105,124,125,191]. This drawback of phase-field methods is due to different factors, depending on the phase-field formulation employed. We discuss this issue first for Cahn-Hilliard-based methods and then for Allen-Cahn-based methods. For Cahn-Hilliard-based methods, the mass conservation of each individual phase is not guaranteed (shrinkage and coarsening phenomena) for two main factors: (i) the chemical potential has no volume-preserving stationary solution for interfaces with finite curvature [126]; (ii) the Cahn-Hilliard fails to satisfy maximum bound principle (MBP) due to the fourth order bi-harmonic operator [348,349]. As a consequence, it is possible to obtain unbounded solutions of the phase field (i.e., undershoots and overshoots) when a double well potential is employed [348–350]. As shown by Yue *et al.* [104], even in the absence of flow, we can have a flux of energy between the two contributions of the free-energy functional, f_0 and f_{mix} , and the total energy can be reduced by shifting the bulk value of the phase field and at the same time reducing the amount of interfacial area [104,301,351] (i.e., the region in which $|\nabla\phi| \neq 0$). This issue can be mitigated adopting one of the strategies reported in Sec. II A: (i) use of penalty fluxes, which further enforce the equilibrium profile [105,111,112]; (ii) use of variable or degenerate mobility coefficients [113–116]; (iii) adoption of dual grid resolution methods [58,117]; (iv) employment of mass redistribution algorithms [123]; (v) modifications to the free-energy functional [125,126].

For Allen-Cahn-based methods, the problem of mass conservation (shrinkage) can be traced back to the presence of curvature-driven motion in the original formulation of the Allen-Cahn equation, and to the way in which the above-mentioned curvature-driven flux is removed to make the Allen-Cahn equation conservative. The formulation which is affected the most by the shrinkage problem is the one relying on time-dependent Lagrangian-multipliers [138,144,352]. Indeed, for the above-mentioned case, only a nonlocal correction is used to satisfy the total mass conservation constraint; however, the diffusion process is a local process that depends on the local value of curvature. For formulations that employ space- and time-dependent Lagrangian multipliers or the conservative version of the Allen-Cahn equations, the curvature-driven motion is removed via local corrections and thus spontaneous shrinkage of interfacial structures characterized by high values of curvature does not occur [93,138,144]. Finally, for formulations that employ the conservative version of the Allen-Cahn equation, this problem should not arise as the curvature-driven flux is canceled out, at least to leading order [92]; in addition, with a proper choice of the discretization scheme, bounded solutions of the phase field can be obtained [93]. Nevertheless, a small mass leakage can still occur when interfacial features with a size comparable to the grid spacing are described.

APPENDIX B: CURVATURE-DRIVEN MOTION AND DERIVATION OF CONSERVATIVE ALLEN-CAHN EQUATION

We discuss here some features of the Allen-Cahn equation. To highlight the curvature-driven motion present in the Allen-Cahn equation, we can start from the following equation that describes an interface moving with a velocity proportional to its curvature, κ , and advected by an external flow field [92,124]:

$$\frac{\partial\phi}{\partial t} + \mathbf{u} \cdot \nabla\phi = b\kappa|\nabla\phi|, \quad (\text{B1})$$

where b is a generic constant and \mathbf{u} is the velocity vector. Recalling that $\mathbf{n} = \nabla\phi/|\nabla\phi|$ is the interface normal vector, the curvature can be written as

$$\kappa = \nabla \cdot \mathbf{n} = \nabla \cdot \left(\frac{\nabla\phi}{|\nabla\phi|} \right) = \frac{1}{|\nabla\phi|} \left[\nabla^2\phi - \frac{\nabla\phi \cdot \nabla|\nabla\phi|}{|\nabla\phi|} \right]. \quad (\text{B2})$$

From the equilibrium profile $\phi_{eq} = \tanh(s/\sqrt{2}\epsilon)$, we also have

$$|\nabla\phi| = \frac{\partial\phi}{\partial s} = \frac{1-\phi^2}{\sqrt{2}\epsilon}; \quad \frac{\nabla\phi \cdot \nabla|\nabla\phi|}{|\nabla\phi|} = \frac{\partial^2\phi}{\partial s^2} = \frac{\phi(\phi^2-1)}{\epsilon^2}. \quad (\text{B3})$$

Upon substitution of the latter expression (second relation) in Eq. (B2), and setting $b = \epsilon^2$, we obtain

$$\frac{\partial\phi}{\partial t} + \mathbf{u} \cdot \nabla\phi = b\kappa|\nabla\phi| = \epsilon^2 \left[\nabla^2\phi - \frac{\phi(\phi^2-1)}{\epsilon^2} \right] = \epsilon^2 \nabla^2\phi - \phi^3 - \phi = \epsilon^2 \nabla^2\phi - f'_0, \quad (\text{B4})$$

where in the last expression the right-hand side of the Allen-Cahn Eq. (5) can be recognized. We can get to similar conclusions using the kernel $\phi_{eq} = [1 + \tanh(s/2\epsilon)]/2$ [93,124], for which we have

$$|\nabla\phi| = \frac{\partial\phi}{\partial s} = \frac{\phi(1-\phi)}{\epsilon}; \quad \frac{\nabla\phi \cdot \nabla|\nabla\phi|}{|\nabla\phi|} = \frac{\partial^2\phi}{\partial s^2} = \frac{\phi(1-\phi)(1-2\phi)}{\epsilon^2}. \quad (\text{B5})$$

From the expressions derived above, Eqs. (B3)–(B5), the conservative form of the Allen-Cahn equation can be derived. To this aim, we substitute in Eq. (B1) the expression for the curvature obtained in Eq. (B2) and we enforce the divergence-free condition on the flow field, obtaining

$$\frac{\partial\phi}{\partial t} + \nabla \cdot (\mathbf{u}\phi) = b \left[\nabla^2\phi - \frac{\nabla\phi \cdot \nabla|\nabla\phi|}{|\nabla\phi|} \right]. \quad (\text{B6})$$

We then remove the curvature-driven motion so that the two terms cancel out at the leading order [92]:

$$\frac{\partial\phi}{\partial t} + \nabla \cdot (\mathbf{u}\phi) = b \left[\nabla^2\phi - \frac{\nabla\phi \cdot \nabla|\nabla\phi|}{|\nabla\phi|} - \kappa|\nabla\phi| \right] = b \left[\nabla^2\phi - \frac{\nabla\phi \cdot \nabla|\nabla\phi|}{|\nabla\phi|} - |\nabla\phi|\nabla \cdot \frac{\nabla\phi}{|\nabla\phi|} \right]. \quad (\text{B7})$$

Using Eq. (B3) for $|\nabla\phi|$, we have

$$\frac{\partial\phi}{\partial t} + \nabla \cdot (\mathbf{u}\phi) = b \left\{ \nabla^2\phi - \frac{\nabla\phi}{|\nabla\phi|} \cdot \nabla \left[\frac{1-\phi^2}{\sqrt{2}\epsilon} \right] - \frac{1-\phi^2}{\sqrt{2}\epsilon} \nabla \cdot \frac{\nabla\phi}{|\nabla\phi|} \right\}, \quad (\text{B8})$$

where, using the chain rule, we have

$$\frac{\partial\phi}{\partial t} + \nabla \cdot (\mathbf{u}\phi) = b \left[\nabla^2\phi - \nabla \cdot \left(\frac{1-\phi^2}{\sqrt{2}\epsilon} \frac{\nabla\phi}{|\nabla\phi|} \right) \right]. \quad (\text{B9})$$

Defining the coefficient $\gamma = b/(\sqrt{2}\epsilon)$, we finally have

$$\frac{\partial\phi}{\partial t} + \nabla \cdot (\mathbf{u}\phi) = \gamma \nabla \cdot \left[\sqrt{2}\epsilon \nabla\phi - \left((1-\phi^2) \frac{\nabla\phi}{|\nabla\phi|} \right) \right], \quad (\text{B10})$$

which is the conservative Allen-Cahn Eq. (14). The expression of the conservative Allen-Cahn equation reported in Mirjalili *et al.* [93] and Chiu and Lin [124] can be obtained using the expression of Eq. (B5) instead of Eq. (B3) as these works assume the kernel $\phi_{eq} = [1 + \tanh(s/2\epsilon)]/2$.

-
- [1] R. A. Shaw, Particle-turbulence interactions in atmospheric clouds, *Annu. Rev. Fluid Mech.* **35**, 183 (2003).
 [2] W. K. Melville, The role of surface-wave breaking in air-sea interaction, *Annu. Rev. Fluid Mech.* **28**, 279 (1996).

- [3] L. Deike, Mass transfer at the ocean-atmosphere interface: The role of wave breaking, droplets, and bubbles, *Annu. Rev. Fluid Mech.* **54**, 191 (2022).
- [4] S. Di Giorgio, S. Pirozzoli, and A. Iafra, On coherent vortical structures in wave breaking, *J. Fluid Mech.* **947**, A44 (2022).
- [5] S. Elghobashi, Direct numerical simulation of turbulent flows laden with droplets or bubbles, *Annu. Rev. Fluid Mech.* **51**, 217 (2019).
- [6] V. Mathai, D. Lohse, and C. Sun, Bubbly and buoyant particle-laden turbulent flows, *Annu. Rev. Condens. Matter Phys.* **11**, 529 (2020).
- [7] G. Soligo, A. Roccon, and A. Soldati, Turbulent flows with drops and bubbles: What numerical simulations can tell us—Freeman scholar lecture, *ASME J. Fluids Eng.* **143**, 080801 (2021).
- [8] Y. Qi, S. Tan, N. Corbitt, C. Urbanik, A. K. Salibindla, and R. Ni, Fragmentation in turbulence by small eddies, *Nat. Commun.* **13**, 469 (2022).
- [9] N. Rui, Deformation and breakup of bubbles and drops in turbulence, [arXiv:2305.18570](https://arxiv.org/abs/2305.18570).
- [10] S. Balachandar, S. Zaleski, A. Soldati, G. Ahmadi, and L. Bourouiba, Host-to-host airborne transmission as a multiphase flow problem for science-based social distance guidelines, *Int. J. Multiphase Flow* **132**, 103439 (2020).
- [11] J. Wang, M. Alipour, G. Soligo, A. Roccon, M. De Paoli, F. Picano, and A. Soldati, Short-range exposure to airborne virus transmission and current guidelines, *Proc. Natl. Acad. Sci. USA* **118**, e2105279118 (2021).
- [12] L. Bourouiba, The fluid dynamics of disease transmission, *Annu. Rev. Fluid Mech.* **53**, 473 (2021).
- [13] N. Reinecke, G. Petritsch, D. Schmitz, and D. Mewes, Tomographic measurement techniques—Visualization of multiphase flows, *Chem. Eng. Technol.* **21**, 7 (1998).
- [14] R. Lindken, L. Gui, and W. Merzkirch, Velocity measurements in multiphase flow by means of particle image velocimetry, *Chem. Eng. Technol.* **22**, 202 (1999).
- [15] R. Lindken and W. Merzkirch, A novel PIV technique for measurements in multiphase flows and its application to two-phase bubbly flows, *Exp. Fluids* **33**, 814 (2002).
- [16] R. Scardovelli and S. Zaleski, Direct numerical simulation of free-surface and interfacial flow, *Annu. Rev. Fluid Mech.* **31** 567 (1999).
- [17] A. Prosperetti and G. Tryggvason, *Computational Methods for Multiphase Flow* (Cambridge University Press, Cambridge, UK, 2009).
- [18] S. Mirjalili, S. S. Jain, and M. S. Dodd, Interface-capturing methods for two-phase flows: An overview and recent developments, *Center Turbul. Res. Annu. Res. Briefs* **117** (2017).
- [19] M. Gorokhovski and M. Herrmann, Modeling primary atomization, *Annu. Rev. Fluid Mech.* **40**, 343 (2008).
- [20] R. S. Rogallo and P. Moin, Numerical simulation of turbulent flows, *Annu. Rev. Fluid Mech.* **16**, 99 (1984).
- [21] P. Moin and K. Mahesh, Direct numerical simulation: A tool in turbulence research, *Annu. Rev. Fluid Mech.* **30**, 539 (1998).
- [22] P. Orlandi, *Fluid Flow Phenomena: A Numerical Toolkit* (Springer Science & Business Media, Cham, 2000), Vol. 55.
- [23] J. Dongarra and P. Luszczek, Top500, in *Encyclopedia of Parallel Computing*, edited by D. Padua (Springer US, Boston, MA, 2011), pp. 2055–2057.
- [24] S. Murad and C. K. Law, Molecular simulation of droplet collision in the presence of ambient gas, *Mol. Phys.* **96**, 81 (1999).
- [25] G. Tryggvason, S. Dabiri, B. Aboulhasanzadeh, and J. Lu, Multiscale considerations in direct numerical simulations of multiphase flows, *Phys. Fluids* **25**, 031302 (2013).
- [26] J. Magiera and C. Rohde, A molecular-continuum multiscale model for inviscid liquid-vapor flow with sharp interfaces, *J. Comput. Phys.* **469**, 111551 (2022).
- [27] J. D. van der Waals, The thermodynamic theory of capillarity under the hypothesis of a continuous variation of density, *J. Stat. Phys.* **20**, 200 (1979).
- [28] V. L. Ginzburg, On the theory of superconductivity, *Il Nuovo Cimento (1955-1965)* **2**, 1234 (1955).

- [29] L. D. Landau and V. Ginzburg, On the theory of superconductivity, *Zh. Eksp. Teor. Fiz.* **20**, 1064 (1950).
- [30] J. Cahn and J. Hilliard, Free energy of a nonuniform system. I. Interfacial free energy, *J. Chem. Phys.* **28**, 258 (1958).
- [31] J. Cahn and J. Hilliard, Free energy of a nonuniform system. II. Thermodynamic basis, *J. Chem. Phys.* **30**, 1121 (1959).
- [32] J. Cahn and J. Hilliard, Free energy of a nonuniform system. III. Nucleation in a two-component incompressible fluid, *J. Chem. Phys.* **31**, 688 (1959).
- [33] S. M. Allen and J. W. Cahn, Mechanisms of phase transformations within the miscibility gap of Fe-rich Fe-Al alloys, *Acta Metall.* **24**, 425 (1976).
- [34] D. Anderson, G. McFadden, and A. Wheeler, Diffuse interface methods in fluid mechanics, *Annu. Rev. Fluid Mech.* **30**, 139 (1998).
- [35] A. G. Lamorgese, D. Molin, and R. Mauri, Phase-field approach to multiphase flow modeling, *Milan J. Math.* **79**, 597 (2011).
- [36] J. Kim, Phase-Field models for multi-component fluid flows, *Commun. Comput. Phys.* **12**, 613 (2012).
- [37] E. W. Hester, L.-A. Couston, B. Favier, K. J. Burns, and G. M. Vasil, Improved phase-field models of melting and dissolution in multicomponent flows, *Proc. Royal Soc. A* **476**, 20200508 (2020).
- [38] R. Yang, K. L. Chong, H.-R. Liu, R. Verzicco, and D. Lohse, Abrupt transition from slow to fast melting of ice, *Phys. Rev. Fluids* **7**, 083503 (2022).
- [39] R. Yang, C. J. Howland, H.-R. Liu, R. Verzicco, and D. Lohse, Morphology evolution of a melting solid layer above its melt heated from below, *J. Fluid Mech.* **956**, A23 (2023).
- [40] F. Ziebert and I. S. Aranson, Computational approaches to substrate-based cell motility, *npj Comput. Mater.* **2**, 16019 (2016).
- [41] L. Metselaar, J. M. Yeomans, and A. Doostmohammadi, Topology and Morphology of Self-Deforming Active Shells, *Phys. Rev. Lett.* **123**, 208001 (2019).
- [42] R. Mueller and A. Doostmohammadi, Phase-field models of active matter, [arXiv:2102.05557](https://arxiv.org/abs/2102.05557).
- [43] W. J. Boettinger, J. A. Warren, C. Beckermann, and A. Karma, Phase-field simulation of solidification, *Annu. Rev. Mater. Res.* **32**, 163 (2002).
- [44] I. Steinbach, Why solidification? Why phase field? *JOM* **65**, 1096 (2013).
- [45] I. Steinbach, Phase-field model for microstructure evolution at the mesoscopic scale, *Annu. Rev. Mater. Res.* **43**, 89 (2013).
- [46] N. Moelans, B. Blanpain, and P. Wollants, An introduction to phase-field modeling of microstructure evolution, *Calphad* **32**, 268 (2008).
- [47] A. A. Wheeler, W. J. Boettinger, and G. B. McFadden, Phase-field model for isothermal phase transitions in binary alloys, *Phys. Rev. A* **45**, 7424 (1992).
- [48] M. J. Borden, C. V. Verhoosel, M. A. Scott, T. J. Hughes, and C. M. Landis, A phase-field description of dynamic brittle fracture, *Comput. Methods Appl. Mech. Eng.* **217-220**, 77 (2012).
- [49] M. Ambati, T. Gerasimov, and L. De Lorenzis, A review on phase-field models of brittle fracture and a new fast hybrid formulation, *Comput. Mech.* **55**, 383 (2015).
- [50] M. R. Tonks, A. Cheniour, and L. Aagesen, How to apply the phase-field method to model radiation damage, *Comput. Mater. Sci.* **147**, 353 (2018).
- [51] H. Emmerich, Advances of and by phase-field modeling in condensed-matter physics, *Adv. Phys.* **57**, 1 (2008).
- [52] S. Vakili, I. Steinbach, and F. Varnik, Multi-phase-field simulation of microstructure evolution in metallic foams, *Sci. Rep.* **10**, 19987 (2020).
- [53] J. Hötzer, A. Reiter, H. Hierl, P. Steinmetz, M. Selzer, and B. Nestler, The parallel multiphysics phase-field framework Pace3D, *J. Comput. Sci.* **26**, 1 (2018).
- [54] Q. Wang, G. Zhang, Y. Li, Z. Hong, D. Wang, and S. Shi, Application of phase-field method in rechargeable batteries, *npj Comput. Mater.* **6**, 176 (2020).
- [55] I. Steinbach, Phase-field models in materials science, *Model. Simul. Mat. Sci. Eng.* **17**, 073001 (2009).
- [56] M. R. Tonks and L. K. Aagesen, The phase-field method: Mesoscale simulation aiding material discovery, *Annu. Rev. Mater. Res.* **49**, 79 (2019).

- [57] D. Jacqmin, Calculation of two-phase Navier-Stokes flows using phase-field modeling, *J. Comput. Phys.* **155**, 96 (1999).
- [58] H.-R. Liu, C. S. Ng, K. L. Chong, D. Lohse, and R. Verzicco, An efficient phase-field method for turbulent multiphase flows, *J. Comput. Phys.* **446**, 110659 (2021).
- [59] A. Vela-Martín and M. Avila, Deformation of drops by outer eddies in turbulence, *J. Fluid Mech.* **929**, A38 (2021).
- [60] A. Vela-Martín and M. Avila, Memoryless drop breakup in turbulence, *Sci. Adv.* **8**, eabp9561 (2022).
- [61] L. Scarbolo, F. Bianco, and A. Soldati, Coalescence and breakup of large droplets in turbulent channel flow, *Phys. Fluids* **27**, 073302 (2015).
- [62] A. E. Komrakova, D. Eskin, and J. Derksen, Numerical study of turbulent liquid-liquid dispersions, *AIChE J.* **61**, 2618 (2015).
- [63] A. Roccon, M. De Paoli, F. Zonta, and A. Soldati, Viscosity-modulated breakup and coalescence of large drops in bounded turbulence, *Phys. Rev. Fluids* **2**, 083603 (2017).
- [64] F. Mangani, G. Soligo, A. Roccon, and A. Soldati, Influence of density and viscosity on deformation, breakage, and coalescence of bubbles in turbulence, *Phys. Rev. Fluids* **7**, 053601 (2022).
- [65] S. Mukherjee, A. Safdari, O. Shardt, S. Kenjereš, and H. E. A. Van den Akker, Droplet-turbulence interactions and quasi-equilibrium dynamics in turbulent emulsions, *J. Fluid Mech.* **878**, 221 (2019).
- [66] I. Giroto, R. Benzi, G. Di Staso, A. Scagliarini, S. F. Schifano, and F. Toschi, Build up of yield stress fluids via chaotic emulsification, *J. Turbul.* **23**, 265 (2022).
- [67] A. Roccon, F. Zonta, and A. Soldati, Turbulent drag reduction by compliant lubricating layer, *J. Fluid Mech.* **863**, R1 (2019).
- [68] A. Roccon, F. Zonta, and A. Soldati, Energy balance in lubricated drag-reduced turbulent channel flow, *J. Fluid Mech.* **911**, A37 (2021).
- [69] G. Giamagas, F. Zonta, A. Roccon, and A. Soldati, Propagation of capillary waves in two-layer oil-water turbulent flow, *J. Fluid Mech.* **960**, A5 (2023).
- [70] *Multiphase Microfluidics: The Diffuse Interface Model*, edited by R. Mauri, CISM International Centre for Mechanical Sciences (Springer, Berlin, 2012).
- [71] D. Molin and R. Mauri, Spinodal decomposition of binary mixtures with composition-dependent heat conductivities, *Chem. Eng. Sci.* **63**, 2402 (2008).
- [72] A. G. Lamorgese and R. Mauri, Nucleation and spinodal decomposition of liquid mixtures, *Phys. Fluids* **17**, 034107 (2005).
- [73] P. Perlekar, R. Benzi, H. J. H. Clercx, D. R. Nelson, and F. Toschi, Spinodal Decomposition in Homogeneous and Isotropic Turbulence, *Phys. Rev. Lett.* **112**, 014502 (2014).
- [74] R. Mauri, R. Shinnar, and G. Triantafyllou, Spinodal decomposition in binary mixtures, *Phys. Rev. E* **53**, 2613 (1996).
- [75] T. Lee and L. Liu, Lattice Boltzmann simulations of micron-scale drop impact on dry surfaces, *J. Comput. Phys.* **229**, 8045 (2010).
- [76] Q. Zhang, T.-Z. Qian, and X.-P. Wang, Phase-field simulation of a droplet impacting a solid surface, *Phys. Fluids* **28**, 022103 (2016).
- [77] A. Badillo, Quantitative phase-field modeling for wetting phenomena, *Phys. Rev. E* **91**, 033005 (2015).
- [78] A. Celani, A. Mazzino, P. Muratore-Ginanneschi, and L. Vozella, Phase-field model for the Rayleigh-Taylor instability of immiscible fluids, *J. Fluid Mech.* **622**, 115 (2009).
- [79] H.-R. Liu, K. L. Chong, C. S. Ng, R. Verzicco, and D. Lohse, Enhancing heat transport in multiphase Rayleigh-Bénard turbulence by changing the plate-liquid contact angles, *J. Fluid Mech.* **933**, R1 (2022).
- [80] M. Laradji, H. Guo, M. Grant, and M. Zuckermann, The effect of surfactants on the dynamics of phase separation, *J. Phys.: Condens. Matter* **4**, 6715 (1992).
- [81] T. Teramoto and F. Yonezawa, Droplet growth dynamics in a water/oil/surfactant system, *J. Colloid Interface Sci.* **235**, 329 (2001).
- [82] S. Engblom, M. Do-Quang, G. Amberg, and A. Tornberg, On diffuse interface modeling and simulation of surfactants in two-phase fluid flow, *Commun. Comput. Phys.* **14**, 879 (2013).
- [83] G. Soligo, A. Roccon, and A. Soldati, Coalescence of surfactant-laden drops by Phase-field method, *J. Comput. Phys.* **376**, 1292 (2019).

- [84] X. Zheng, H. Babaei, S. Dong, C. Chrysosostomidis, and G. Karniadakis, A phase-field method for 3D simulation of two-phase heat transfer, *Int. J. Heat Mass Transf.* **82**, 282 (2015).
- [85] S. Mirjalili, S. S. Jain, and A. Mani, A computational model for interfacial heat and mass transfer in two-phase flows using a phase-field method, *Int. J. Heat Mass Transf.* **197**, 123326 (2022).
- [86] A. Badillo, Quantitative phase-field modeling for boiling phenomena, *Phys. Rev. E* **86**, 041603 (2012).
- [87] W. Verdier, P. Kestener, and A. Cartalade, Performance portability of lattice Boltzmann methods for two-phase flows with phase change, *Comput. Methods Appl. Mech. Eng.* **370**, 113266 (2020).
- [88] Z. Wang, X. Zheng, C. Chrysosostomidis, and G. E. Karniadakis, A phase-field method for boiling heat transfer, *J. Comput. Phys.* **435**, 110239 (2021).
- [89] M. Reder, D. Schneider, F. Wang, S. Daubner, and B. Nestler, Phase-field formulation of a fictitious domain method for particulate flows interacting with complex and evolving geometries, *Int. J. Numer. Methods Fluids* **93**, 2486 (2021).
- [90] G. Lecrivain, Y. Kotani, R. Yamamoto, U. Hampel, and T. Taniguchi, Diffuse interface model to simulate the rise of a fluid droplet across a cloud of particles, *Phys. Rev. Fluids* **3**, 094002 (2018).
- [91] A. Hajisharifi, C. Marchioli, and A. Soldati, Interface topology and evolution of particle patterns on deformable drops in turbulence, *J. Fluid Mech.* **933**, A41 (2022).
- [92] Y. Sun and C. Beckermann, Sharp interface tracking using the phase-field equation, *J. Comput. Phys.* **220**, 626 (2007).
- [93] S. Mirjalili, C. B. Ivey, and A. Mani, A conservative diffuse interface method for two-phase flows with provable boundedness properties, *J. Comput. Phys.* **401**, 109006 (2020).
- [94] R. Aris, *Vectors, Tensors and the Basic Equations of Fluid Mechanics* (Dover Publications, Mineola, NY, 1989).
- [95] Z. Guo and P. Lin, A thermodynamically consistent phase-field model for two-phase flows with thermocapillary effects, *J. Fluid Mech.* **766**, 226 (2015).
- [96] S. Mirjalili and A. Mani, Consistent, energy-conserving momentum transport for simulations of two-phase flows using the phase-field equations, *J. Comput. Phys.* **426**, 109918 (2021).
- [97] E. Albin, R. Knikker, S. Xin, C. O. Paschereit, and Y. d'Angelo, Computational assessment of curvatures and principal directions of implicit surfaces from 3D scalar data, in *Mathematical Methods for Curves and Surfaces: 9th International Conference, MMCS 2016, Tønsberg, Norway, June 23–28, 2016, Revised Selected Papers 9* (Springer, Berlin, 2017), pp. 1–22.
- [98] C. Hirt and B. Nichols, Volume of fluid (VOF) method for the dynamics of free boundaries, *J. Comput. Phys.* **39**, 201 (1981).
- [99] V. Badalassi, H. Ceniceròs, and S. Banerjee, Computation of multiphase systems with phase-field models, *J. Comput. Phys.* **190**, 371 (2003).
- [100] P. Yue, J. Feng, C. Liu, and J. Shen, A diffuse-interface method for simulating two-phase flows of complex fluids, *J. Fluid Mech.* **515**, 293 (2004).
- [101] A. Hajisharifi, C. Marchioli, and A. Soldati, Particle capture by drops in turbulent flow, *Phys. Rev. Fluids* **6**, 024303 (2021).
- [102] P. Yue, C. Zhou, and J. Feng, Sharp-interface limit of the Cahn-Hilliard model for moving contact lines, *J. Fluid Mech.* **645**, 279 (2010).
- [103] Alternative phase-field formulations employ the values $\phi = 0$ and $\phi = 1$ to distinguish the two pure phases. In this case, the corresponding expression of the double well potential is $f_0 = \phi^2(\phi - 1)^2/2$ and the corresponding equilibrium profile is $\phi_{eq} = [1 + \tanh(s/2\epsilon)]/2$.
- [104] P. Yue, C. Zhou, and J. Feng, Spontaneous shrinkage of drops and mass conservation in phase-field simulations, *J. Comput. Phys.* **223**, 1 (2007).
- [105] G. Soligo, A. Roccon, and A. Soldati, Mass-conservation-improved phase-field methods for turbulent multiphase flow simulation, *Acta Mech.* **230**, 683 (2019).
- [106] J. Kim, K. Kang, and J. Lowengrub, Conservative multigrid methods for Cahn-Hilliard fluids, *J. Comput. Phys.* **193**, 511 (2004).
- [107] M. Bagheri, B. Stumpf, I. V. Roisman, A. Davdand, M. Wörner, and H. Marschall, A unified finite volume framework for phase-field simulations of an arbitrary number of fluid phases, *Can. J. Chem. Eng.* **100**, 2291 (2022).

- [108] H. W. Zheng, C. Shu, and Y. T. Chew, Lattice Boltzmann interface capturing method for incompressible flows, *Phys. Rev. E* **72**, 056705 (2005).
- [109] H. Zheng, C. Shu, and Y.-T. Chew, A lattice Boltzmann model for multiphase flows with large density ratio, *J. Comput. Phys.* **218**, 353 (2006).
- [110] L. Scarbolo and A. Soldati, Turbulence modulation across the interface of a large deformable drop, *J. Turbul.* **14**, 27 (2013).
- [111] Y. Li, J. Choi, and J. Kim, A phase-field fluid modeling and computation with interfacial profile correction term, *Commun. Nonlin. Sci.* **30**, 84 (2016).
- [112] Y. Zhang and W. Ye, A flux-corrected phase-field method for surface diffusion, *Commun. Comput. Phys.* **22**, 422 (2017).
- [113] H. D. Ceniceros and C. J. García-Cervera, A new approach for the numerical solution of diffusion equations with variable and degenerate mobility, *J. Comput. Phys.* **246**, 1 (2013).
- [114] C. M. Elliott and H. Garcke, On the Cahn-Hilliard equation with degenerate mobility, *SIAM J. Math. Anal.* **27**, 404 (1996).
- [115] C. Liu, On the convective Cahn-Hilliard equation with degenerate mobility, *J. Math. Anal. Appl.* **344**, 124 (2008).
- [116] S. Dai, Q. Liu, T. Luong, and K. Promislow, On nonnegative solutions for the functionalized Cahn-Hilliard equation with degenerate mobility, *Res. Appl. Math.* **12**, 100195 (2021).
- [117] H. Ding and C. Yuan, On the diffuse interface method using a dual-resolution Cartesian grid, *J. Comput. Phys.* **273**, 243 (2014).
- [118] H. D. Ceniceros, R. L. Nos, and A. M. Roma, Three-dimensional, fully adaptive simulations of phase-field fluid models, *J. Comput. Phys.* **229**, 6135 (2010).
- [119] A. Fakhari, D. Bolster, and L.-S. Luo, A weighted multiple-relaxation-time lattice Boltzmann method for multiphase flows and its application to partial coalescence cascades, *J. Comput. Phys.* **341**, 22 (2017).
- [120] M. A. Khanwale, A. D. Lofquist, H. Sundar, J. A. Rossmannith, and B. Ganapathysubramanian, Simulating two-phase flows with thermodynamically consistent energy stable Cahn-Hilliard Navier-Stokes equations on parallel adaptive octree based meshes, *J. Comput. Phys.* **419**, 109674 (2020).
- [121] M. A. Khanwale, K. Saurabh, M. Fernando, V. M. Calo, H. Sundar, J. A. Rossmannith, and B. Ganapathysubramanian, A fully coupled framework for solving Cahn-Hilliard Navier-Stokes equations: Second-order, energy-stable numerical methods on adaptive octree based meshes, *Comput. Phys. Commun.* **280**, 108501 (2022).
- [122] S. Ham, Y. Li, D. Jeong, C. Lee, S. Kwak, Y. Hwang, and J. Kim, An explicit adaptive finite difference method for the Cahn-Hilliard equation, *J. Nonlin. Sci.* **32**, 80 (2022).
- [123] Y. Wang, C. Shu, J. Shao, J. Wu, and X. Niu, A mass-conserved diffuse interface method and its application for incompressible multiphase flows with large density ratio, *J. Comput. Phys.* **290**, 336 (2015).
- [124] P.-H. Chiu and Y.-T. Lin, A conservative phase-field method for solving incompressible two-phase flows, *J. Comput. Phys.* **230**, 185 (2011).
- [125] M. Kwakkel, M. Fernandino, and C. A. Dorao, A redefined energy functional to prevent mass loss in phase-field methods, *AIP Adv.* **10**, 065124 (2020).
- [126] A. Dadvand, M. Bagheri, N. Samkhaniani, H. Marschall, and M. Wörner, Advected phase-field method for bounded solution of the Cahn-Hilliard Navier-Stokes equations, *Phys. Fluids* **33**, 053311 (2021).
- [127] R. Folch, J. Casademunt, A. Hernández-Machado, and L. Ramírez-Piscina, Phase-field model for heleshaw flows with arbitrary viscosity contrast. II. Numerical study, *Phys. Rev. E* **60**, 1734 (1999).
- [128] E. P. Van Der Poel, R. Ostilla-Mónico, J. Donners, and R. Verzicco, A pencil distributed finite difference code for strongly turbulent wall-bounded flows, *Comput. Fluids* **116**, 10 (2015).
- [129] P. Costa, A fft-based finite-difference solver for massively parallel direct numerical simulations of turbulent flows, *Comput. Math. with Appl.* **76**, 1853 (2018).
- [130] M. Geier, A. Fakhari, and T. Lee, Conservative phase-field lattice Boltzmann model for interface tracking equation, *Phys. Rev. E* **91**, 063309 (2015).
- [131] F. Ren, B. Song, M. C. Sukop, and H. Hu, Improved lattice Boltzmann modeling of binary flow based on the conservative Allen-Cahn equation, *Phys. Rev. E* **94**, 023311 (2016).

- [132] H. L. Wang, Z. H. Chai, B. C. Shi, and H. Liang, Comparative study of the lattice Boltzmann models for Allen-Cahn and Cahn-Hilliard equations, *Phys. Rev. E* **94**, 033304 (2016).
- [133] S. Watanabe and T. Aoki, Large-scale flow simulations using lattice Boltzmann method with AMR following free-surface on multiple GPUs, *Comput. Phys. Commun.* **264**, 107871 (2021).
- [134] C. Schwarzmeier, M. Holzer, T. Mitchell, M. Lehmann, F. Häusl, and U. Rude, Comparison of free-surface and conservative Allen-Cahn phase-field lattice Boltzmann method, *J. Comput. Phys.* **473**, 111753 (2023).
- [135] S. Saito, M. Yoshino, and K. Suzuki, Numerical simulation of bubbly flows by the improved lattice Boltzmann method for incompressible two-phase flows, *Comput. Fluids* **254**, 105797 (2023).
- [136] M. Brassel and E. Bretin, A modified phase-field approximation for mean curvature flow with conservation of the volume, *Math. Methods Appl. Sci.* **34**, 1157 (2011).
- [137] D. Lee and J. Kim, Comparison study of the conservative Allen-Cahn and the Cahn-Hilliard equations, *Math. Comput. Simul.* **119**, 35 (2016).
- [138] J. Kim, S. Lee, and Y. Choi, A conservative Allen-Cahn equation with a space-time dependent Lagrange multiplier, *Int. J. Eng. Sci.* **84**, 11 (2014).
- [139] V. Joshi and R. K. Jaiman, A positivity preserving and conservative variational scheme for phase-field modeling of two-phase flows, *J. Comput. Phys.* **360**, 137 (2018).
- [140] D. Jeong and J. Kim, Conservative Allen-Cahn–Navier-Stokes system for incompressible two-phase fluid flows, *Comput. Fluids* **156**, 239 (2017).
- [141] S. Zhai, Z. Weng, and X. Feng, Investigations on several numerical methods for the nonlocal Allen-Cahn equation, *Int. J. Heat Mass Transf.* **87**, 111 (2015).
- [142] Z. Huang, G. Lin, and A. M. Ardekani, Consistent and conservative scheme for incompressible two-phase flows using the conservative Allen-Cahn model, *J. Comput. Phys.* **420**, 109718 (2020).
- [143] Z. Huang, G. Lin, and A. M. Ardekani, Consistent, essentially conservative and balanced-force phase-field method to model incompressible two-phase flows, *J. Comput. Phys.* **406**, 109192 (2020).
- [144] Z. Chai, D. Sun, H. Wang, and B. Shi, A comparative study of local and nonlocal Allen-Cahn equations with mass conservation, *Int. J. Heat Mass Transf.* **122**, 631 (2018).
- [145] M. Alfaro and P. Alifrangis, Convergence of a mass conserving Allen-Cahn equation whose Lagrange multiplier is nonlocal and local, *Interfaces Free Bound.* **16**, 243 (2014).
- [146] C. Beckermann, H.-J. Diepers, I. Steinbach, A. Karma, and X. Tong, Modeling melt convection in phase-field simulations of solidification, *J. Comput. Phys.* **154**, 468 (1999).
- [147] Please note that the conservative Allen-Cahn equation has been here rewritten using the equilibrium kernel $\phi_{\text{eq}} = \tanh(s/\sqrt{2}\epsilon)$ while in the original derivation of Chiu and Lin [124] the kernel $\phi_{\text{eq}} = [1 + \tanh(s/2\epsilon)]/2$ is employed. As a result, the coefficients and the second term on the right-hand side are slightly different. Please refer to Appendix B for the complete derivation of the conservative Allen-Cahn equation.
- [148] E. Olsson and G. Kreiss, A conservative level set method for two phase flow, *J. Comput. Phys.* **210**, 225 (2005).
- [149] E. Olsson, G. Kreiss, and S. Zahedi, A conservative level set method for two phase flow II, *J. Comput. Phys.* **225**, 785 (2007).
- [150] T. Biben, C. Misbah, A. Leyrat, and C. Verdier, An advected-field approach to the dynamics of fluid interfaces, *Europhys. Lett.* **63**, 623 (2003).
- [151] T. Waławczyk, A consistent solution of the re-initialization equation in the conservative level-set method, *J. Comput. Phys.* **299**, 487 (2015).
- [152] R. Chiodi and O. Desjardins, A reformulation of the conservative level set reinitialization equation for accurate and robust simulation of complex multiphase flows, *J. Comput. Phys.* **343**, 186 (2017).
- [153] P.-H. Chiu, A coupled phase-field framework for solving incompressible two-phase flows, *J. Comput. Phys.* **392**, 115 (2019).
- [154] S. S. Jain, Accurate conservative phase-field method for simulation of two-phase flows, *J. Comput. Phys.* **469**, 111529 (2022).
- [155] S. S. Jain, A. Mani, and P. Moin, A conservative diffuse-interface method for compressible two-phase flows, *J. Comput. Phys.* **418**, 109606 (2020).

- [156] C. Hirt, J. Cook, and T. Butler, A Lagrangian method for calculating the dynamics of an incompressible fluid with free surface, *J. Comput. Phys.* **5**, 103 (1970).
- [157] G. Ryskin and L. Leal, Numerical solution of free-boundary problems in fluid mechanics. Part 1. The finite-difference technique, *J. Fluid Mech.* **148**, 1 (1984).
- [158] G. Ryskin and L. Leal, Numerical solution of free-boundary problems in fluid mechanics. Part 2. Buoyancy-driven motion of a gas bubble through a quiescent liquid, *J. Fluid Mech.* **148**, 19 (1984).
- [159] F. Zonta, A. Soldati, and M. Onorato, Growth and spectra of gravity-capillary waves in countercurrent air/water turbulent flow, *J. Fluid Mech.* **777**, 245 (2015).
- [160] J. Glimm, Tracking of interfaces for fluid flow: Accurate methods for piecewise smooth problems, in *Transonic, Shock, and Multidimensional Flows* (Academic Press, San Diego, CA, 1982), pp. 259–287.
- [161] J. Glimm and O. A. McBryan, A computational model for interfaces, *Adv. Appl. Math.* **6**, 422 (1985).
- [162] H. S. Udaykumar, H. C. Kan, W. Shyy, and R. Tran-Son-Tay, Multiphase dynamics in arbitrary geometries on fixed cartesian grids, *J. Comput. Phys.* **137**, 366 (1997).
- [163] R. Fedkiw, T. Aslam, B. Merriman, and S. Osher, A nonoscillatory Eulerian approach to interfaces in multimaterial flows (the ghost fluid method), *J. Comput. Phys.* **152**, 457 (1999).
- [164] L. Lee and R. J. LeVeque, An immersed interface method for incompressible Navier-Stokes equations, *SIAM J. Sci. Comput.* **25**, 832 (2003).
- [165] J.-M. Hong, T. Shinar, M. Kang, and R. Fedkiw, On boundary condition capturing for multiphase interfaces, *J. Sci. Comput.* **31**, 99 (2007).
- [166] The interface normal vector is here defined as $\mathbf{n} = \nabla\phi/|\nabla\phi|$ and the curvature as $\kappa = \nabla \cdot \mathbf{n}$. Using this convention, to obtain a consistent implementation of the resulting pressure jump in the Navier-Stokes equations a negative sign is required on the surface tension term. Alternatively, one can also choose to orient the interface normal arbitrarily (e.g., outward) and update accordingly the sign of the source term present in the Navier-Stokes equations to maintain consistency.
- [167] C. S. Peskin, Flow patterns around heart valves: A numerical method, *J. Comput. Phys.* **10**, 252 (1972).
- [168] S. Popinet, Numerical models of surface tension, *Annu. Rev. Fluid Mech.* **50**, 49 (2018).
- [169] J. U. Brackbill, D. B. Kothe, and C. Zemach, A continuum method for modeling surface tension, *J. Comput. Phys.* **100**, 335 (1992).
- [170] B. Lafaurie, C. Nardone, R. Scardovelli, S. Zaleski, and G. Zanetti, Modelling merging and fragmentation in multiphase flows with SURFER, *J. Comput. Phys.* **113**, 134 (1994).
- [171] D. Gueyffier, J. Li, A. Nadim, R. Scardovelli, and S. Zaleski, Volume-of-fluid interface tracking with smoothed surface stress methods for three-dimensional flows, *J. Comput. Phys.* **152**, 423 (1999).
- [172] M. Sussman, P. Smereka, and S. Osher, A level set approach for computing solutions to incompressible two-phase flow, *J. Comput. Phys.* **114**, 146 (1994).
- [173] J. Kim, A continuous surface tension force formulation for diffuse-interface models, *J. Comput. Phys.* **204**, 784 (2005).
- [174] M. W. Williams, D. B. Kothe, and E. G. Puckett, Accuracy and convergence of continuum surface tension models, in *Fluid Dynamics at Interfaces*, edited by W. Shy (Cambridge University Press, Cambridge, MA, 1999), pp. 347–356.
- [175] J. Helmsen, Non-convex profile evolution in two dimensions using volume of fluids, *LBNL Tech. Rep. LBNL-40693*, Lawrence National Laboratory, Berkeley, CA (1997).
- [176] B. D. Nichols, C. W. Hirt, and R. S. Hotchkiss, SOLA-VOF: A solution algorithm for transient fluid flow with multiple free boundaries, *Technical Report N 81* (1980).
- [177] M. D. Torrey, L. D. Cloutman, R. C. Mjolsness, and C. W. Hirt, NASA-VOF2D: A computer program for incompressible flows with free surfaces, *Technical Report N 86* (1985).
- [178] Y. Renardy and M. Renardy, Prost: a parabolic reconstruction of surface tension for the volume-of-fluid method, *J. Comput. Phys.* **183**, 400 (2002).
- [179] F. Evrard, F. Denner, and B. van Wachem, Estimation of curvature from volume fractions using parabolic reconstruction on two-dimensional unstructured meshes, *J. Comput. Phys.* **351**, 271 (2017).
- [180] M. Coquerelle and S. Glockner, A fourth-order accurate curvature computation in a level set framework for two-phase flows subjected to surface tension forces, *J. Comput. Phys.* **305**, 838 (2016).

- [181] S. Mirjalili, M. A. Khanwale, and A. Mani, Assessment of an energy-based surface tension model for simulation of two-phase flows using second-order phase-field methods, *J. Comput. Phys.* **474**, 111795 (2023).
- [182] H. Yuan, Z. Chen, C. Shu, Y. Wang, X. Niu, and S. Shu, A free energy-based surface tension force model for simulation of multiphase flows by level-set method, *J. Comput. Phys.* **345**, 404 (2017).
- [183] A. A. Howard and A. M. Tartakovsky, A conservative level set method for n-phase flows with a free-energy-based surface tension model, *J. Comput. Phys.* **426**, 109955 (2021).
- [184] R. van der Sman and S. van der Graaf, Diffuse interface model of surfactant adsorption onto flat and droplet interfaces, *Rheol. Acta* **46**, 3 (2006).
- [185] A. Yun, Y. Li, and J. Kim, A new phase-field model for a water-oil-surfactant system, *Appl. Math. Comput.* **229**, 422 (2014).
- [186] M. O. Abu-Al-Saud, S. Popinet, and H. A. Tchelepi, A conservative and well-balanced surface tension model, *J. Comput. Phys.* **371**, 896 (2018).
- [187] M. M. Francois, S. J. Cummins, E. D. Dendy, D. B. Kothe, J. M. Sicilian, and M. W. Williams, A balanced-force algorithm for continuous and sharp interfacial surface tension models within a volume tracking framework, *J. Comput. Phys.* **213**, 141 (2006).
- [188] M. Wörner, Numerical modeling of multiphase flows in microfluidics and micro process engineering: A review of methods and applications, *Microfluid. Nanofluid.* **12**, 841 (2012).
- [189] L. Scarbolo, D. Molin, P. Perlekar, M. Sbragaglia, A. Soldati, and F. Toschi, Unified framework for a side-by-side comparison of different multicomponent algorithms: Lattice Boltzmann vs. phase-field model, *J. Comput. Phys.* **234**, 263 (2013).
- [190] F. O. Alpak, B. Riviere, and F. Frank, A phase-field method for the direct simulation of two-phase flows in pore-scale media using a nonequilibrium wetting boundary condition, *Comput. Geosci.* **20**, 881 (2016).
- [191] H. Ding, P. Spelt, and C. Shu, Diffuse interface model for incompressible two-phase flows with large density ratios, *J. Comput. Phys.* **226**, 2078 (2007).
- [192] Similar expressions can be derived employing the equilibrium kernel $\phi_{\text{eq}} = [1 + \tanh(s/2\epsilon)]/2$. In this case, $\phi = 0$ and $\phi = 1$ are the bulk values for the identification of the two phases, and density and viscosity maps read as $\rho(\phi) = \rho_1\phi + \rho_2(1 - \phi)$ and $\eta(\phi) = \eta_1\phi + \eta_2(1 - \phi)$.
- [193] S. Dong and J. Shen, A time-stepping scheme involving constant coefficient matrices for phase-field simulations of two-phase incompressible flows with large density ratios, *J. Comput. Phys.* **231**, 5788 (2012).
- [194] C. Liu and J. Shen, A phase-field model for the mixture of two incompressible fluids and its approximation by a fourier-spectral method, *Phys. D: Nonlin. Phenom.* **179**, 211 (2003).
- [195] V. Khatavkar, P. Anderson, P. Duineveld, and H. Meijer, Diffuse-interface modelling of droplet impact, *J. Fluid Mech.* **581**, 97 (2007).
- [196] F. Boyer, A theoretical and numerical model for the study of incompressible mixture flows, *Comput. Fluids* **31**, 41 (2002).
- [197] S. Mirjalili, C. B. Ivey, and A. Mani, Comparison between the diffuse interface and volume of fluid methods for simulating two-phase flows, *Int. J. Multiphase Flow* **116**, 221 (2019).
- [198] J. Shen and X. Yang, A phase-field model and its numerical approximation for two-phase incompressible flows with different densities and viscosities, *SIAM J. Sci. Comput.* **32**, 1159 (2010).
- [199] Z. Wang, S. Dong, M. S. Triantafyllou, Y. Constantinides, and G. E. Karniadakis, A stabilized phase-field method for two-phase flow at high Reynolds number and large density/viscosity ratio, *J. Comput. Phys.* **397**, 108832 (2019).
- [200] C. Zhan, Z. Chai, and B. Shi, Consistent and conservative phase-field-based lattice Boltzmann method for incompressible two-phase flows, *Phys. Rev. E* **106**, 025319 (2022).
- [201] Z. Huang, G. Lin, and A. M. Ardekani, A consistent and conservative phase-field model for thermo-gas-liquid-solid flows including liquid-solid phase change, *J. Comput. Phys.* **449**, 110795 (2022).
- [202] J. Kamp, J. Villwock, and M. Kraume, Drop coalescence in technical liquid/liquid applications: a review on experimental techniques and modeling approaches, *Rev. Chem. Eng.* **33**, 1 (2017).

- [203] G. D. M. Mackay and S. Mason, The gravity approach and coalescence of fluid drops at liquid interfaces, *Can. J. Chem. Eng.* **41**, 203 (1963).
- [204] M. Loewenberg and E. Hinch, Collision of two deformable drops in shear flow, *J. Fluid Mech.* **338**, 299 (1997).
- [205] C. Gotaas, P. Havelka, H. Jakobsen, H. Svendsen, M. Hase, N. Roth, and B. Weigand, Effect of viscosity on droplet-droplet collision outcome: Experimental study and numerical comparison, *Phys. Fluids* **19**, 102106 (2007).
- [206] N. Chen, T. Kuhl, R. Tadmor, Q. Lin, and J. Israelachvili, Large Deformations During the Coalescence of Fluid Interfaces, *Phys. Rev. Lett.* **92**, 024501 (2004).
- [207] S. Perumanath, M. K. Borg, M. V. Chubynsky, J. E. Sprittles, and J. M. Reese, Droplet Coalescence is Initiated by Thermal Motion, *Phys. Rev. Lett.* **122**, 104501 (2019).
- [208] D. G. Aarts, M. Schmidt, and H. N. W. Lekkerkerker, Direct visual observation of thermal capillary waves, *Science* **304**, 847 (2004).
- [209] D. G. A. L. Aarts, H. N. W. Lekkerkerker, H. Guo, G. H. Wegdam, and D. Bonn, Hydrodynamics of Droplet Coalescence, *Phys. Rev. Lett.* **95**, 164503 (2005).
- [210] A. N. Zdravkov, G. W. M. Peters, and H. E. H. Meijer, Film drainage and interfacial instabilities in polymeric systems with diffuse interfaces, *J. Colloid Interface Sci.* **296**, 86 (2006).
- [211] G. Soligo, A. Roccon, and A. Soldati, Breakage, coalescence, and size distribution of surfactant-laden droplets in turbulent flow, *J. Fluid Mech.* **881**, 244 (2019).
- [212] M. Dodd and A. Ferrante, On the interaction of Taylor length scale size droplets and isotropic turbulence, *J. Fluid Mech.* **806**, 356 (2016).
- [213] M. Rosti, F. De Vita, and L. Brandt, Numerical simulations of emulsions in shear flows, *Acta Mech.* **230**, 667 (2019).
- [214] M. Rosti, Z. Ge, S. Jain, M. Dodd, and L. Brandt, Droplets in homogeneous shear turbulence, *J. Fluid Mech.* **876**, 962 (2019).
- [215] A. Soldati and P. Andreussi, The influence of coalescence on droplet transfer in vertical annular flow, *Chem. Eng. Sci.* **51**, 353 (1996).
- [216] N. Ashgriz and J. Poo, Coalescence and separation in binary collisions of liquid drops, *J. Fluid Mech.* **221**, 183 (1990).
- [217] J. Ruiz-Rus, P. Ern, V. Roig, and C. Martínez-Bazán, Coalescence of bubbles in a high Reynolds number confined swarm, *J. Fluid Mech.* **944**, A13 (2022).
- [218] P. Yue, J. Feng, C. Liu, and J. Shen, Diffuse-interface simulations of drop coalescence and retraction in viscoelastic fluids, *J. Non-Newton. Fluid* **129**, 163 (2005).
- [219] M. Liu and D. Bothe, Toward the predictive simulation of bouncing versus coalescence in binary droplet collisions, *Acta Mech* **230**, 623 (2019).
- [220] L. Rekvig and D. Frenkel, Molecular simulations of droplet coalescence in oil/water/surfactant systems, *J. Chem. Phys.* **127**, 134701 (2007).
- [221] K.-L. Pan, C. K. Law, and B. Zhou, Experimental and mechanistic description of merging and bouncing in head-on binary droplet collision, *J. Appl. Phys.* **103**, 064901 (2008).
- [222] S. Thomas, A. Esmaeeli, and G. Tryggvason, Multiscale computations of thin films in multiphase flows, *Int. J. Multiphase Flow* **36**, 71 (2010).
- [223] G. Tryggvason, J. Thomas, S. Lu, and B. Aboulhasanzadeh, Multiscale issues in DNS of multiphase flows, *Acta Math. Sci.* **30**, 551 (2010).
- [224] G. E. Charles and S. G. Mason, The coalescence of liquid drops with flat liquid/liquid interfaces, *J. Colloid Sci.* **15**, 236 (1960).
- [225] R. S. Allan, G. E. Charles, and S. G. Mason, The approach of gas bubbles to a gas/liquid interface, *J. Colloid Sci.* **16**, 150 (1961).
- [226] F. De Vita, M. E. Rosti, S. Caserta, and L. Brandt, On the effect of coalescence on the rheology of emulsions, *J. Fluid Mech.* **880**, 969 (2019).
- [227] A. Montessori, M. Lauricella, N. Tirelli, and S. Succi, Mesoscale modelling of near-contact interactions for complex flowing interfaces, *J. Fluid Mech.* **872**, 327 (2019).

- [228] M. Talley, M. Zimmer, and I. Bolotnov, Coalescence prevention algorithm for level-set method, *J. Fluid Eng. T. ASME* **139**, 081301 (2017).
- [229] M. Kwakkel, W.-P. Breugem, and B. Boersma, Extension of a CLSVOF method for droplet-laden flows with a coalescence/breakup model, *J. Comput. Phys.* **253**, 166 (2013).
- [230] C. Körner, M. Thies, T. Hofmann, N. Thürey, and U. Rude, Lattice Boltzmann model for free surface flow for modeling foaming, *J. Stat. Phys.* **121**, 179 (2005).
- [231] C. Körner, Foam formation mechanisms in particle suspensions applied to metal foams, *Mater. Sci. Eng. A* **495**, 227 (2008).
- [232] R. Benzi, M. Sbragaglia, A. Scagliarini, P. Perlekar, M. Bernaschi, S. Succi, and F. Toschi, Internal dynamics and activated processes in soft-glassy materials, *Soft Matter* **11**, 1271 (2015).
- [233] B. Dollet, A. Scagliarini, and M. Sbragaglia, Two-dimensional plastic flow of foams and emulsions in a channel: Experiments and lattice Boltzmann simulations, *J. Fluid Mech.* **766**, 556 (2015).
- [234] Y. P. Sitompul, T. Aoki, and T. Takaki, Simulation of turbulent bubbly pipe flow with high density ratio and high Reynolds number by using the lattice Boltzmann method and a multi-phase-field model, *Int. J. Multiphase Flow* **134**, 103505 (2021).
- [235] A. Yamanaka, T. Takaki, T. Aoki, and T. Shimokawabe, Multi-phase-field simulation of austenite-to-ferrite transformation accelerated by GPU computing, *J. Comput. Sci. Technol.* **6**, 182 (2012).
- [236] P. Karnakov, F. Wermelinger, S. Litvinov, and P. Koumoutsakos, Aphros: High performance software for multiphase flows with large scale bubble and drop clusters, in *Proceedings of the Platform for Advanced Scientific Computing Conference* (ACM Press, New York, NY, 2020), pp. 1–10.
- [237] P. Karnakov, S. Litvinov, J. M. Favre, and P. Koumoutsakos, Breaking waves: To foam or not to foam? *Phys. Rev. Fluids* **5**, 110503 (2020).
- [238] P. Notz and O. Basaran, Dynamics and breakup of a contracting liquid filament, *J. Fluid Mech.* **512**, 223 (2004).
- [239] C. R. Anthony, P. M. Kamat, M. T. Harris, and O. A. Basaran, Dynamics of contracting filaments, *Phys. Rev. Fluids* **4**, 093601 (2019).
- [240] J. Eggers, Theory of drop formation, *Phys. Fluids* **7**, 941 (1995).
- [241] J. Eggers, Nonlinear dynamics and breakup of free-surface flows, *Rev. Mod. Phys.* **69**, 865 (1997).
- [242] J. Lu and G. Tryggvason, Direct numerical simulations of multifluid flows in a vertical channel undergoing topology changes, *Phys. Rev. Fluids* **3**, 084401 (2018).
- [243] J. Lu and G. Tryggvason, Multifluid flows in a vertical channel undergoing topology changes: Effect of void fraction, *Phys. Rev. Fluids* **4**, 084301 (2019).
- [244] M. Herrmann, On simulating primary atomization using the refined level set grid method, *At. Sprays* **21**, 283 (2011).
- [245] F. Evrard, F. Denner, and B. van Wachem, A multi-scale approach to simulate atomization processes, *Intl. J. Multiphase Flow* **119**, 194 (2019).
- [246] M. Herrmann, Detailed numerical simulations of the primary atomization of a turbulent liquid jet in crossflow, *J. Eng. Gas Turbul. Power* **132**, 061506 (2010).
- [247] Y. Ling, S. Zaleski, and R. Scardovelli, Multiscale simulation of atomization with small droplets represented by a Lagrangian point-particle model, *Int. J. Multiphase Flow* **76**, 122 (2015).
- [248] D. Kim, O. Desjardins, M. Herrmann, and P. Moin, Toward two-phase simulation of the primary breakup of a round liquid jet by a coaxial flow of gas, *Center Turbul. Res. Ann. Res. Briefs* 185 (2006).
- [249] G. Tomar, D. Fuster, S. Zaleski, and S. Popinet, Multiscale simulations of primary atomization, *Comput. Fluids* **39**, 1864 (2010).
- [250] S. Apte, M. Gorokhovski, and P. Moin, LES of atomizing spray with stochastic modeling of secondary breakup, *Int. J. Multiphase Flow* **29**, 1503 (2003).
- [251] M. Herrmann, Modeling primary breakup: A three-dimensional Eulerian level set/vortex sheet method for two-phase interface dynamics, *Center Turbul. Res. Ann. Res. Briefs* 185 (2003).
- [252] Although the work of Mukherjee *et al.* [65] relies on a pseudopotential lattice Boltzmann formulation (PP-LB), the method resembles in many aspects phase-field formulations, and thus it has been classified as PFM.

- [253] M. Crialesi-Esposito, S. Chibbaro, and L. Brandt, The interaction of droplet dynamics and turbulence cascade, *Commun. Phys.* **6**, 5 (2023).
- [254] G. Deane and M. Stokes, Scale dependence of bubble creation mechanisms in breaking waves, *Nature (London)* **418**, 839 (2002).
- [255] C. E. Blenkinsopp and J. R. Chaplin, Bubble size measurements in breaking waves using optical fiber phase detection probes, *IEEE J. Ocean. Engng.* **35**, 388 (2010).
- [256] A. H. Callaghan, M. D. Stokes, and G. B. Deane, The effect of water temperature on air entrainment, bubble plumes, and surface foam in a laboratory breaking-wave analog, *J. Geophys. Res. Oceans* **119**, 7463 (2014).
- [257] Z. Wang, J. Yang, and F. Stern, High-fidelity simulations of bubble, droplet and spray formation in breaking waves, *J. Fluid Mech.* **792**, 307 (2016).
- [258] L. Deike, W. Melville, and S. Popinet, Air entrainment and bubble statistics in breaking waves, *J. Fluid Mech.* **801**, 91 (2016).
- [259] W. Mostert, S. Popinet, and L. Deike, High-resolution direct simulation of deep water breaking waves: Transition to turbulence, bubbles, and droplets production, *J. Fluid Mech.* **942**, A27 (2022).
- [260] C. Garrett, M. Li, and D. Farmer, The connection between bubble size spectra and energy dissipation rates in the upper ocean, *J. Phys. Oceanogr.* **30**, 2163 (2000).
- [261] A. N. Kolmogorov, The local structure of turbulence in incompressible viscous fluid for very large Reynolds numbers, *Proc. Math. Phys. Eng. Sci.* **434**, 9 (1991).
- [262] J. Hinze, Fundamentals of the hydrodynamic mechanism of splitting in dispersion processes, *AIChE J.* **1**, 289 (1955).
- [263] W. H. R. Chan, P. L. Johnson, and P. Moin, The turbulent bubble break-up cascade. Part 1. Theoretical developments, *J. Fluid Mech.* **912**, A42 (2021).
- [264] W. H. R. Chan, P. L. Johnson, P. Moin, and J. Urzay, The turbulent bubble break-up cascade. Part 2. Numerical simulations of breaking waves, *J. Fluid Mech.* **912**, A43 (2021).
- [265] X. Gao, J. Chen, Y. Qiu, Y. Ding, and J. Xie, Effect of phase change on jet atomization: A direct numerical simulation study, *J. Fluid Mech.* **935**, A16 (2022).
- [266] H. Duguid and J. Stampfer Jr., The evaporation rates of small, freely falling water drops, *J. Atmos. Sci.* **28**, 1233 (1971).
- [267] J. Lu, M. Muradoglu, and G. Tryggvason, Effect of insoluble surfactant on turbulent bubbly flows in vertical channels, *Int. J. Multiphase Flow* **95**, 135 (2017).
- [268] I. Roghair, M. V. S. Annaland, and J. Kuipers, An improved front-tracking technique for the simulation of mass transfer in dense bubbly flows, *Chem. Eng. Sci.* **152**, 351 (2016).
- [269] M. İrfan and M. Muradoglu, A front tracking method for direct numerical simulation of evaporation process in a multiphase system, *J. Comput. Phys.* **337**, 132 (2017).
- [270] D. Bothe, M. Koebe, K. Wielage, J. Prüss, and H.-J. Warnecke, *Direct Numerical Simulation of Mass Transfer between Rising Gas Bubbles and Water* (Springer, Berlin, 2004), pp. 159–174.
- [271] A. Alke and D. Bothe, 3D numerical modeling of soluble surfactant at fluidic interfaces based on the volume-of-fluid method, *Fluid Dyn. Mater. Process* **5**, 345 (2009).
- [272] N. Scapin, P. Costa, and L. Brandt, A volume-of-fluid method for interface-resolved simulations of phase-changing two-fluid flows, *J. Comput. Phys.* **407**, 109251 (2020).
- [273] B. M. Ningegowda, Z. Ge, G. Lupo, L. Brandt, and C. Duwig, A mass-preserving interface-correction level set/ghost fluid method for modeling of three-dimensional boiling flows, *Int. J. Heat Mass Transf.* **162**, 120382 (2020).
- [274] J. Xu, A level-set method for interfacial flows with surfactant, *J. Comput. Phys.* **212**, 590 (2006).
- [275] D. L. Albernaz, M. Do-Quang, J. C. Hermanson, and G. Amberg, Droplet deformation and heat transfer in isotropic turbulence, *J. Fluid Mech.* **820**, 61 (2017).
- [276] Z. Dong, W. Li, and Y. Song, A numerical investigation of bubble growth on and departure from a superheated wall by lattice Boltzmann method, *Int. J. Heat Mass Transf.* **53**, 4908 (2010).
- [277] H. Safari, M. H. Rahimian, and M. Krafczyk, Extended lattice Boltzmann method for numerical simulation of thermal phase change in two-phase fluid flow, *Phys. Rev. E* **88**, 013304 (2013).

- [278] A. Begmohammadi, M. Farhadzadeh, and M. H. Rahimian, Simulation of pool boiling and periodic bubble release at high density ratio using lattice Boltzmann method, *Int. Commun. Heat Mass Transf.* **61**, 78 (2015).
- [279] Q. He, W. Huang, Y. Yin, D. Li, and Y. Wang, A lattice Boltzmann model for liquid-vapor-solid flow with thermal phase change, *Comput. Math. Appl.* **114**, 60 (2022).
- [280] G. K. Batchelor, Small-scale variation of convected quantities like temperature in turbulent fluid Part 1. General discussion and the case of small conductivity, *J. Fluid Mech.* **5**, 113 (1959).
- [281] G. K. Batchelor, I. D. Howells, and A. A. Townsend, Small-scale variation of convected quantities like temperature in turbulent fluid Part 2. The case of large conductivity, *J. Fluid Mech.* **5**, 134 (1959).
- [282] V. G. Levich and R. J. Seeger, Physicochemical hydrodynamics, *Am. J. Phys.* **31**, 892 (1963).
- [283] L. Scriven and C. Sterlino, The Marangoni effects, *Nature (London)* **187**, 186 (1960).
- [284] B. Dai and L. Leal, The mechanism of surfactant effects on drop coalescence, *Phys. Fluids* **20**, 040802 (2008).
- [285] S. Narayan, I. Makhnenko, D. B. Moravec, B. G. Hauser, A. J. Dallas, and C. S. Dutcher, Insights into the microscale coalescence behavior of surfactant-stabilized droplets using a microfluidic hydrodynamic trap, *Langmuir* **36**, 9827 (2020).
- [286] I. Kralova and J. Sjöblom, Surfactants used in food industry: A review, *J. Disper. Sci. Technol.* **30**, 1363 (2009).
- [287] S. Takagi and Y. Matsumoto, Surfactant effects on bubble motion and bubbly flows, *Annu. Rev. Fluid Mech.* **43**, 615 (2011).
- [288] M. Rosen and J. Kunjappu, *Surfactants and Interfacial Phenomena* (John Wiley & Sons, New York, NY, 2012).
- [289] R. Pereira, I. Ashton, B. Sabbaghzadeh, J. Shutler, and R. Upstill-Goddard, Reduced air-sea CO₂ exchange in the Atlantic Ocean due to biological surfactants, *Nat. Geosci.* **11**, 492 (2018).
- [290] H. Manikantan and T. M. Squires, Surfactant dynamics: Hidden variables controlling fluid flows, *J. Fluid Mech.* **892**, P1 (2020).
- [291] H. A. Stone, A simple derivation of the time-dependent convective-diffusion equation for surfactant transport along a deforming interface, *Phys. Fluids A* **2**, 111 (1990).
- [292] S. Komura and H. Kodama, Two-order-parameter model for an oil-water-surfactant system, *Phys. Rev. E* **55**, 1722 (1997).
- [293] R. Gupta, R. Mauri, and R. Shinnar, Phase separation of liquid mixtures in the presence of surfactants, *Ind. Eng. Chem. Res.* **38**, 2418 (1999).
- [294] M. Muradoglu and G. Tryggvason, A front-tracking method for computation of interfacial flows with soluble surfactants, *J. Comput. Phys.* **227**, 2238 (2008).
- [295] M. Muradoglu and G. Tryggvason, Simulations of soluble surfactants in 3D multiphase flow, *J. Comput. Phys.* **274**, 737 (2014).
- [296] Y. Renardy, M. Renardy, and V. Cristini, A new volume-of-fluid formulation for surfactants and simulations of drop deformation under shear at a low viscosity ratio, *Eur. J. Mech. B Fluids* **21**, 49 (2002).
- [297] A. James and J. Lowengrub, A surfactant-conserving volume-of-fluid method for interfacial flows with insoluble surfactant, *J. Comput. Phys.* **201**, 685 (2004).
- [298] J. Xu, Y. Yang, and J. Lowengrub, A level-set continuum method for two-phase flows with insoluble surfactant, *J. Comput. Phys.* **231**, 5897 (2012).
- [299] J. Xu and W. Ren, A level-set method for two-phase flows with moving contact line and insoluble surfactant, *J. Comput. Phys.* **263**, 71 (2014).
- [300] K. Erik Teigen, P. Song, J. Lowengrub, and A. Voigt, A diffuse-interface method for two-phase flows with soluble surfactants, *J. Comput. Phys.* **230**, 375 (2011).
- [301] R. G. van der Sman and S. Van der Graaf, Emulsion droplet deformation and breakup with lattice Boltzmann model, *Comput. Phys. Commun.* **178**, 492 (2008).
- [302] C.-H. Teng, I.-L. Chern, and M.-C. Lai, Simulating binary fluid-surfactant dynamics by a phase-field model, *Discrete Contin. Dyn. Syst. B* **17**(4), 1289 (2012).

- [303] H. Liu and Y. Zhang, Phase-field modeling droplet dynamics with soluble surfactants, *J. Comput. Phys.* **229**, 9166 (2010).
- [304] Y. Li and J. Kim, A comparison study of phase-field models for an immiscible binary mixture with surfactant, *Eur. J. Phys. B.* **85**, 340 (2012).
- [305] O. Theissen and G. Gompper, Lattice-Boltzmann study of spontaneous emulsification, *Eur. Phys. J. B* **11**, 91 (1999).
- [306] L. Yi, C. Wang, T. v. Vuren, D. Lohse, F. Risso, F. Toschi, and C. Sun, Physical mechanisms for droplet size and effective viscosity asymmetries in turbulent emulsions, *J. Fluid Mech.* **951**, A39 (2022).
- [307] N. Young, J. S. Goldstein, and M. Block, The motion of bubbles in a vertical temperature gradient, *J. Fluid Mech.* **6**, 350 (1959).
- [308] L. Liggieri, A. Sanfeld, and A. Steinchen, Effects of magnetic and electric fields on surface tension of liquids, *Physica A* **206**, 299 (1994).
- [309] S. H. Davis, Thermocapillary instabilities, *Annu. Rev. Fluid Mech.* **19**, 403 (1987).
- [310] H. Kou, W. Li, X. Zhang, N. Xu, X. Zhang, J. Shao, J. Ma, Y. Deng, and Y. Li, Temperature-dependent coefficient of surface tension prediction model without arbitrary parameters, *Fluid Phase Equilib.* **484**, 53 (2019).
- [311] A. Chesters and I. Bazhlekoy, Effect of insoluble surfactants on drainage and rupture of a film between drops interacting under a constant force, *J. Colloid Interface Sci.* **230**, 229 (2000).
- [312] V. G. Levich and V. S. Krylov, Surface tension-driven phenomena, *Annu. Rev. Fluid Mech.* **1**, 293 (1969).
- [313] H. C. Kuhlmann, *Thermocapillary Convection in Models of Crystal Growth* (Springer, Berlin, 1999), p. 152.
- [314] P. S. Sánchez, J. M. Ezquerro, J. Porter, J. Fernández, and I. Tinao, Effect of thermocapillary convection on the melting of phase change materials in microgravity: Experiments and simulations, *Int. J. Heat Mass Transf.* **163**, 120478 (2020).
- [315] M. F. Schatz and G. P. Neitzel, Experiments on thermocapillary instabilities, *Annu. Rev. Fluid Mech.* **33**, 93 (2001).
- [316] A. Alke, D. Bothe, M. Kroege, and H. Warnecke, VOF-based simulation of conjugate mass transfer from freely moving fluid particles, *Computat. Meth. Multiph. Flow* **63**, 157 (2009).
- [317] D. Bothe and S. Fleckenstein, A volume-of-fluid-based method for mass transfer processes at fluid particles, *Chem. Eng. Sci.* **101**, 283 (2013).
- [318] S. Mirjalili, S. Jain, and A. Mani, Modeling heat and mass transfer across interfaces in two-phase flows using phase-field methods, *Center Turbul. Res. Ann. Res. Briefs* 327 (2020).
- [319] S. Mirjalili, M. Khanwale, and A. Mani, Consistent modeling of scalar transport in multiphase flows using conservative phase field methods, *Center Turbul. Res. Ann. Res. Briefs* 167 (2022).
- [320] V. Mehdi-Nejad, J. Mostaghimi, and S. Chandra, Modelling heat transfer in two-fluid interfacial flows, *Int. J. Numer. Methods Eng.* **61**, 1028 (2004).
- [321] D. Deising, D. Bothe, and H. Marschall, Direct numerical simulation of mass transfer in bubbly flows, *Comput. Fluids* **172**, 524 (2018).
- [322] C. Yang and Z.-S. Mao, Numerical simulation of interphase mass transfer with the level set approach, *Chem. Eng. Sci.* **60**, 2643 (2005).
- [323] J. Wang, P. Lu, Z. Wang, C. Yang, and Z.-S. Mao, Numerical simulation of unsteady mass transfer by the level set method, *Chem. Eng. Sci.* **63**, 3141 (2008).
- [324] K. Kentheswaran, N. Dietrich, S. Tanguy, and B. Lalanne, Direct numerical simulation of gas-liquid mass transfer around a spherical contaminated bubble in the stagnant-cap regime, *Int. J. Heat Mass Transf.* **198**, 123325 (2022).
- [325] Z. Huang, G. Lin, and A. M. Ardekani, A consistent and conservative model and its scheme for n-phase-m-component incompressible flows, *J. Comput. Phys.* **434**, 110229 (2021).
- [326] J. Kou, A. Salama, and X. Wang, Thermodynamically consistent phase-field modelling of activated solute transport in binary solvent fluids, *J. Fluid Mech.* **955**, A41 (2023).
- [327] M. R. Davidson and M. Rudman, Volume-of-fluid calculation of heat or mass transfer across deforming interfaces in two-fluid flow, *Numer. Heat Transf. B: Fundam.* **41**, 291 (2002).

- [328] H. Marschall, K. Hinterberger, C. Schüler, F. Habla, and O. Hinrichsen, Numerical simulation of species transfer across fluid interfaces in free-surface flows using openfoam, *Chem. Eng. Sci.* **78**, 111 (2012).
- [329] The transport equations for the two scalars have been here derived using the equilibrium kernel $\phi_{eq} = \tanh(s/\sqrt{2}\epsilon)$ while in the work of Mirjalili *et al.* [85], equations are derived using the kernel $\phi_{eq} = [1 + \tanh(s/2\epsilon)]/2$.
- [330] S. S. Jain and A. Mani, A computational model for transport of immiscible scalars in two-phase flows, *J. Comput. Phys.* **476**, 111843 (2023).
- [331] Y. Nagata, K. Usui, and M. Bonn, Molecular Mechanism of Water Evaporation, *Phys. Rev. Lett.* **115**, 236102 (2015).
- [332] M. Ishii and T. Hibiki, *Thermo-Fluid Dynamics of Two-phase Flow* (Springer Science & Business Media, Cham, 2010).
- [333] The sign of the surface tension term is reported in literature either with the positive or negative sign. The reason behind this apparent variability is the different conventions of the interface normal vector orientation and computation of the curvature. Here we use the same convection employed in Sec. III.
- [334] C. R. Kharangate and I. Mudawar, Review of computational studies on boiling and condensation, *Int. J. Heat Mass Transf.* **108**, 1164 (2017).
- [335] D. Juric and G. Tryggvason, Computations of boiling flows, *Int. J. Multiphase Flow* **24**, 387 (1998).
- [336] S. W. Welch and J. Wilson, A volume of fluid based method for fluid flows with phase change, *J. Comput. Phys.* **160**, 662 (2000).
- [337] S. Hardt and F. Wondra, Evaporation model for interfacial flows based on a continuum-field representation of the source terms, *J. Comput. Phys.* **227**, 5871 (2008).
- [338] F. Gibou, L. Chen, D. Nguyen, and S. Banerjee, A level set based sharp interface method for the multiphase incompressible Navier–Stokes equations with phase change, *J. Comput. Phys.* **222**, 536 (2007).
- [339] S. Tanguy, T. Ménard, and A. Berlemont, A level set method for vaporizing two-phase flows, *J. Comput. Phys.* **221**, 837 (2007).
- [340] C. Shao, K. Luo, M. Chai, H. Wang, and J. Fan, A computational framework for interface-resolved DNS of simultaneous atomization, evaporation, and combustion, *J. Comput. Phys.* **371**, 751 (2018).
- [341] C. Shao, T. Jin, and K. Luo, The interaction between droplet evaporation and turbulence with interface-resolved direct numerical simulation, *Phys. Fluids* **34**, 072102 (2022).
- [342] A. Rajkotwala, A. Panda, E. Peters, M. Baltussen, C. van der Geld, J. Kuerten, and J. Kuipers, A critical comparison of smooth and sharp interface methods for phase transition, *Int. J. Multiphase Flow* **120**, 103093 (2019).
- [343] N. Scapin, F. Dalla Barba, G. Lupo, M. E. Rosti, C. Duwig, and L. Brandt, Finite-size evaporating droplets in weakly compressible homogeneous shear turbulence, *J. Fluid Mech.* **934**, A15 (2022).
- [344] L. G. Martinez, B. Duret, J. Reveillon, and F. Demoulin, Vapor mixing in turbulent vaporizing flows, *Int. J. Multiphase Flow* **161**, 104388 (2023).
- [345] M. S. Lee, A. Riaz, and V. Aute, Direct numerical simulation of incompressible multiphase flow with phase change, *J. Comput. Phys.* **344**, 381 (2017).
- [346] A. Tamura and K. Katono, Development of a phase-field method for phase change simulations using a conservative Allen-Cahn equation, *ASME J. Nucl. Rad Sci.* **8**, 021401 (2022).
- [347] K. Saurabh, M. Ishii, M. A. Khanwale, H. Sundar, and B. Ganapathysubramanian, Scalable adaptive algorithms for next-generation multiphase flow simulations, in *Proceedings of the IEEE International Parallel and Distributed Processing Symposium (IPDPS)* (IEEE, Piscataway, NJ, 2023), pp. 590–601.
- [348] J. Li, L. Ju, Y. Cai, and X. Feng, Unconditionally maximum bound principle preserving linear schemes for the conservative Allen-Cahn equation with nonlocal constraint, *J. Comput. Sci. Technol.* **87**, 98 (2021).
- [349] M. H. Protter and H. F. Weinberger, *Maximum Principles in Differential Equations* (Springer Science & Business Media, Cham, 2012).

- [350] Q. Du, L. Ju, X. Li, and Z. Qiao, Maximum bound principles for a class of semilinear parabolic equations and exponential time-differencing schemes, [SIAM Rev. **63**, 317 \(2021\)](#).
- [351] T. Waławczyk, On a relation between the volume of fluid, level-set and phase-field interface models, [Int. J. Multiphase Flow **97**, 60 \(2017\)](#).
- [352] J. Rubinstein and P. Sternberg, Nonlocal reaction-diffusion equations and nucleation, [IMA J. Appl. Math. **48**, 249 \(1992\)](#).